The Stress-Memory Effect of Fracture Stiffness During Cyclic Loading in Low-Permeability Sandstone

Kluge, Christian; Blöcher, Guido; Hofmann, Hannes ; Barnhoorn, Auke; Schmittbuhl, Jean; Bruhn, David

DOI
10.1029/2020JB021469

Publication date
2021

Document Version
Final published version

Published in
Journal of Geophysical Research: Solid Earth

Citation (APA)
Kluge, C., Blöcher, G., Hofmann, H., Barnhoorn, A., Schmittbuhl, J., & Bruhn, D. (2021). The Stress-Memory Effect of Fracture Stiffness During Cyclic Loading in Low-Permeability Sandstone. *Journal of Geophysical Research: Solid Earth*, *126*(10), 1-23. Article e2020JB021469. https://doi.org/10.1029/2020JB021469

JGR Solid Earth

RESEARCH ARTICLE

10.1029/2020JB021469

The Stress-Memory Effect of Fracture Stiffness During Cyclic Loading in Low-Permeability Sandstone

Christian Kluge[1,2], **Guido Blöcher**[1,3], **Hannes Hofmann**[1], **Auke Barnhoorn**[2], **Jean Schmittbuhl**[3], and **David Bruhn**[1,2]

[1]Department of Geoenergy, Helmholtz Centre Potsdam GFZ German Research Centre for Geosciences, Potsdam, Germany, [2]Department of Geoscience and Engineering, Delft University of Technology, Delft, The Netherlands, [3]Institute de Physique du Globe de Strasbourg, Strasbourg, France

Key Points:

- Cyclic loading experiments with fractured sandstone to investigate the evolution of fracture closure, permeability and specific stiffness
- Demonstration of a stress-memory effect of fracture stiffness during progressive loading, similar to the "Kaiser Effect" in intact rocks
- Progressive cyclic loading possibly leads to less permeability reduction compared to continuous cyclic loading

Correspondence to:

C. Kluge,
christian.kluge@gfz-potsdam.de

Citation:

Kluge, C., Blöcher, G., Hofmann, H., Barnhoorn, A., Schmittbuhl, J., & Bruhn, D. (2021). The stress-memory effect of fracture stiffness during cyclic loading in low-permeability sandstone. *Journal of Geophysical Research: Solid Earth*, *126*, e2020JB021469. https://doi.org/10.1029/2020JB021469

Received 2 DEC 2020
Accepted 26 SEP 2021

Abstract

The hydraulic performance and mechanical stability of open fractures are crucial for several subsurface applications including fractured geothermal reservoirs or nuclear waste repositories. Their hydraulic and mechanical properties (fluid flow and fracture stiffness) are both strongly dependent on the fracture geometry. Any change in effective stress impacts aperture and thus the ability of fractures to promote flow. Here, we carried out flow experiments with shear displaced tensile fractures in pre-loaded, low-permeability sandstones with two different cyclic loading scenarios with up to 60 MPa hydrostatic confining pressure. During "constant cyclic loading" (CCL) experiments, the fracture was repeatedly loaded to the same peak stress (up to 60 MPa). During "progressive cyclic loading" (PCL) experiments, the confining pressure was progressively increased in each cycle (up to 15, 30, 45, and 60 MPa). The matrix and fracture deformation was monitored using axial and circumferential LVDT extensometers to obtain the fracture stiffness. The fracture geometry before and after the experiment was compared by calculating the aperture distribution from 3D surface scans. Initial loading with confining pressure of the fracture leads to a linear fracture specific stiffness evolution. For any subsequent stress cycles fracture stiffness shifts to a nonlinear behavior. The transition is shown to be related to a stress memory effect, similar to the "Kaiser Effect" for acoustic emissions. PCL of fractures possibly leads to less permeability reduction compared to continuous cyclic loading.

Plain Language Summary

This study describes a set of experiments carried out in a high-pressure compression apparatus to determine hydro-mechanical properties of fractured sandstone samples at cyclic loading conditions. The aim of such experiments is to reproduce pressure conditions in several kilometers depths. The results of this study enable to better understand physical processes within fractures in the deep subsurface. The main focus of this work was to determine the evolution of fracture stiffness and permeability for two different loading scenarios. Here, we were able to determine the stress-memory effect of fracture stiffness. It is shown by a change of the fracture stiffness when exceeding its previous maximum stress level and demonstrates that ancient stress levels are preserved within fractures. Furthermore, we found that progressive cyclic loading of a fracture can better preserve fracture permeability compared to continuous loading conditions. This is crucial for subsurface engineering applications, such as geothermal reservoirs, in order to maintain a sufficient permeability to extend the lifetime of a reservoir.

1. Introduction

The performance of geothermal and petroleum reservoirs, as well as the safety of underground constructions such as nuclear waste repositories, depends on the ability of fractures to either promote or inhibit fluid flow. In addition, the stability of faults and fractures during hydraulic stimulation requires information on how to minimize and mitigate the risks of induced seismicity (Hofmann et al., 2018) or the loss of the hydraulic integrity of the subsurface (Pyrak-Nolte & Nolte, 2016). Coupled hydro-mechanical processes during stress-related deformation of fractures remain notoriously difficult to predict especially in complex fractured rock masses (Rutqvist, 2015). Besides, the evolution of stress over time changes either short-term or at geological time scales and strongly governs the exploration strategies in geothermal reservoirs. Laboratory experiments can be used to develop tools and knowledge about how to characterize fractured rock mass to better predict the hydraulic properties of rocks.

The memory of rocks is described as the capacity of rocks to retain “imprints” from their stress history (Lavrov, 2005). Rocks contain crucial information about the stress history during non-elastic deformation. Loading a rock to a large stress level generates damage or microcracks within the rock. This level of stress can be identified by reloading the rock above the previous stress level (Lockner, 1993), while monitoring acoustic emissions. Acoustic emissions will be present when exceeding the “ancient” stress level. This is known as the “Kaiser Effect” (Kaiser, 1953). It is important to understand if other mechanisms than the generation of microscopic fractures in an intact rock (Holcomb, 1993) lead to a stress memory effect (Lavrov, 2003). In particular, we try to assess here if existing fractures could contain information about their stress history since they behave non-elastically over a larger range of stress owing to the damage of their asperities (Bandis et al., 1983).

Bandis et al. (1983) evaluated the mechanical behavior of fractures during cyclic loading. Since then, a large number of data have been published that study in detail the evolution of fracture closure and permeability during cyclic normal loading (e.g., Z. Chen et al., 2000; Cook, 1992; Hofmann et al., 2016; Kluge et al., 2020; Milsch et al., 2016; Watanabe et al., 2009). The loading path in most of these experiments comprises multiple loading cycles to the same peak load. Such experiments allow for a qualitative description of the changes in physical properties by a repetition of the same loading path. This is important in understanding the performance of a reservoir during different injection and production scenarios (Kluge, Blöcher, Barnhoorn, Schmittbuhl, & Bruhn, 2021). Cyclic loading experiments contain more information when varying the stress path of each loading cycle. The pore fluid pressure oscillations technique can be used to analyze the frictional stability of the fault and to analyze the transition from stable to unstable slip by progressively increasing the magnitude of pore fluid pressure from one cycle to another (Noël et al., 2019). This technique can also be implemented by loading the sample with an increasing external confining pressure with the same differential stress through the different cycles, instead of increasing pore fluid pressure at a constant confining stress.

The hydro-mechanical properties of fractures depend on fracture contact area, fracture size, fracture roughness, and loading stress history (Wang & Cardenas, 2016). These physical factors also control the stiffness of a fracture (Pyrak-Nolte & Morris, 2000). The normal stiffness describes how much a fracture closes when being subjected to an increasing normal load with respect to the normal plane. Generally, normal fracture stiffness evolves exponentially with load (Bandis et al., 1983). Two different models are usually applied to characterize fracture stiffness from laboratory experiments: (a) The fracture stiffness characteristic, χ, which is a parameter that is based on the semi-log closure model for a single loading cycle (Zangerl et al., 2008). It can be used to quantify changes of stiffness in a series of repetitive stress cycles (e.g., Bandis et al., 1983; Crawford et al., 2016; Kluge et al., 2020). In particular, it is useful to describe strain-hardening effects of fractures. However, this parameter is strongly based on a specific model, the semi-log model and can be poorly assessed if the model is not correctly describing the behavior of fractured rock. (b) The specific fracture stiffness, κ, is defined as the ratio of the increment of stress to the increment of displacement caused by a change of the void space in the fracture (Pyrak-Nolte & Morris, 2000). It was shown numerically and experimentally, that it depends on the elastic properties, the fracture geometry, and stress history (e.g., Cook, 1992; Marache et al., 2008; Petrovitch et al., 2013; Pyrak-Nolte & Morris, 2000; Wang & Cardenas, 2016). This property enables to monitor dynamic changes of fracture stiffness for complex stress paths.

Similar to the fracture stiffness, fracture permeability also depends on these parameters. Cyclic loading experiments on hydro-mechanical responses of fractured rocks have a long history and have provided a large number of data (e.g., Z. Chen et al., 2000; Hofmann et al., 2016; Milsch et al., 2016; Watanabe et al., 2009). These studies have focused on a repetition of periodic loading cycles with the same peak stress. Studies with aperture or permeability measurements during non-periodic cyclic loading tests where the cycle's maximum stress is increased from cycle to cycle gained little attention in the past (Lavrov, 2005). Bandis et al. (1983) and Pyrak-Nolte and Morris (2000) showed that larger apertures and therefore more permeable fractures were more compliant than fractures with initially lower aperture and permeability. The question is, whether the mechanical (stiffness) and hydraulic properties (permeability) of fractured rocks are dependent on stress history and if stress cycling alters this relationship (Pyrak-Nolte & Morris, 2000; Pyrak-Nolte & Nolte, 2016). The fracture closure and stiffness are also expected to depend on fracture surface roughness (Akarapu et al., 2011; Persson, 2007). This can only be shown by means of the specific fracture stiffness, κ.

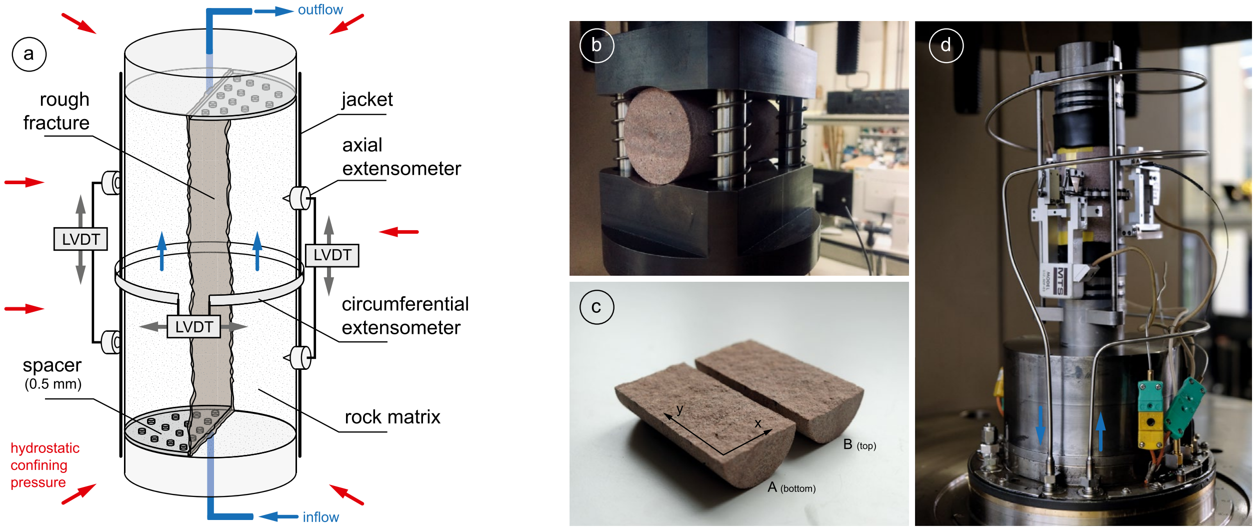

Figure 1. The experimental set-up of the flow-through experiments (a), the Brazilian test set-up for fracture generation (b), the resulting fracture surfaces (c), and the photograph of the experimental set-up.

The deformation of asperities at the fracture surface may lead to changes in the fracture topography and consequently the aperture. Previous studies showed difficulties to quantify changes of fracture topography (e.g., Bandis et al., 1983; Vogler et al., 2016; Xia et al., 2003; Yoshioka, 1994; Zou et al., 2020). Further, it is not clear if potential topography changes affect the self-affine scaling properties, such as the power spectral density (Schmittbuhl, Schmitt, & Scholz, 1995; Schmittbuhl, Vilotte, & Roux, 1995), of fracture surfaces. A combination of measuring the fracture stiffness and permeability during cyclic loading experiments with a progressively increasing stress magnitude together with measurements of the fracture roughness evolution might enable to better understand the dependency of these properties and their relation to the stress history.

In this paper, we present results from a set of laboratory experiments on fractured rock samples with a single displaced tensile fracture, being cyclically loaded using two different loading scenarios: constant cyclic loading (CCL) and progressive cyclic loading (PCL). We will first review the experimental results and analyze the fracture stiffness and fracture permeability evolution. These will be discussed in respect of a possible memory effect of fracture stiffness, similar to that in intact rock during plastic deformation. We then elaborate how this impacts the relationship of the hydraulic-mechanical properties of a fracture under cyclic loading conditions and investigate possible fracture deformation mechanisms.

2. Materials and Methods

2.1. Testing Equipment

The flow-through experiments were carried out in a conventional MTS tri-axial compression cell. The stiff, servo-controlled loading frame (MTS 815, Material Testing Systems Corporation) holds a loading capacity of up to 4,600 kN (load cell calibrated to 2,000 kN, calibration error <1%) and a servo-controlled maximum hydrostatic confining pressure of 140 MPa applied via an oil-filled pressure vessel coupled to an external pressure intensifier. The pore fluid pressure was applied via four Quizix fluid pressure pumps (Model C6000-10K-HC-AT) with a maximum fluid pressure of 69.7 MPa. The differential fluid pressure, which is the difference between in- and outflow pressure, was measured using a differential pressure transducer (GP:50, Model 215; range: 1 MPa; line pressure max. 69.7 MPa; precision: ~1%). The circumferential strain was measured using an LVDT extensometer chain and the axial strain was measured with two axial LVDT extensometers (Figure 1). All experiments have been performed at a temperature of 30 C. Temperature was controlled via heat stripes on the outer side of the loading vessel. During confining pressure increase and decrease the temperature of the confining oil increases and decreases, respectively, due to the Joule-Thomson effect. Data were recorded at a frequency of 1 Hz. A detailed description of the machine can be found in Pei et al. (2016).

Table 1
List of Samples, Intact Sample Dimensions, and Test Types

Sample ID	L, d (mm)	ϕ (%)	k_0 [m^2]	d (mm)	Type
SBT6-BE-04-03	100.18, 49.93	5.86	$3.62 \cdot 10^{-15}$	0.5	CCL
SBT6-BE-04-09	100.12, 49.88	5.16	$2.75 \cdot 10^{-15}$	0.5	PCL
SBT6-BE-04-10	100.12, 49.90	5.31	$1.59 \cdot 10^{-15}$	0.5	PCL

Note. L: sample length, d: sample diameter, ϕ: porosity, k_0: initial sample permeability. d: fracture offset, CCL: constant cyclic loading, PCL: progressive cyclic loading.

2.2. Sample Material

The Flechtingen Sandstone (SBT6-BE) was taken from a quarry near Magdeburg in the North German Basin (Germany) and is a Permian, arkosic litharenite with quartz, feldspars, rock fragments of mainly volcanic origin, about 8% of clay, predominantly illite and chlorite Hassanzadegan et al. (2014). This Rotliegend rock is used as an analogue to the sedimentary geothermal reservoirs in the Northern German Basin (Blöcher et al., 2014, 2016; Hassanzadegan et al., 2012). Grain size is between 0.05 and 0.2 mm for quartz and 0.05–0.1 mm for feldspar. All grains are partly rounded and well sorted. No microfractures were found in our samples. The porosity, ϕ, was measured using the Archimedes principle. The initial sample permeability, k_0, was measured using Darcy's law at 2 MPa confining pressure (Table 1). The low porosity and permeability results from a dense packing of grains, as well as illite partially blocking the pore space by coating the quartz grains. On some grain contacts quartz dissolution occurred, which additionally reduced permeability. The sandstone samples were slightly layered characterized by grain size differences. All cores were taken perpendicular to the bedding. A list of samples and their respective properties is given in Table 1.

2.3. Experimental Procedure

The experimental procedure is composed of four steps: (a) pre-conditioning of samples under hydrostatic pressure conditions to remove the plastic strain, (b) tensile fracture generation using the Brazilian Disk test and surface scanning, (c) imposed rigid shear of the unloaded sample, (d) fracture flow experiment under CCL and PCL conditions. The measured properties are the pressure-dependent rock matrix permeability, the rock matrix porosity, the fracture surface geometry including aperture distribution and roughness, as well as the pressure-dependent fracture closure and fracture permeability.

2.3.1. Sample Pre-Conditioning

To remove the plastic strain of the intact rock samples, all cores were preloaded to a hydrostatic confining pressure of 65 MPa in seven loading cycles. The intact samples were jacketed in a heat-shrink tube and placed into the MTS triaxial cell. One circumferential and two axial LVDT extensometers recorded the lateral, axial, and volumetric strain during the experiment. First, a hydrostatic confining pressure of 2 MPa was applied while the sample was saturated with distilled water under vacuum conditions of about 1 kPa for 24 h. The maximum pore fluid pressure was kept at 0.2 MPa during the entire pre-loading stage. At this point, the permeability of the unloaded sample was measured (Table 1). We applied a continuous inflow rate, Q, and a constant fluid pressure at the sample outlet, p_{out} of 0.2 MPa. From the pressure difference, $\Delta p_p = p_{in} - p_{out}$, the inflow area, A, the temperature-dependent fluid viscosity, μ, and the sample length, L, we calculated the sample permeability, k_s, using Darcy's law (Darcy, 1856):

$$k_s = \frac{Q}{A} \frac{\mu L}{\Delta p_p} \tag{1}$$

Once permeability was measured, the constant inflow rate was changed to a constant pressure mode. By applying a constant fluid pressure of 0.2 MPa at both sides of the sample using only one pump, we measured the pore volume changes during loading. For pre-conditioning, a hydrostatic stress of 65 MPa was applied in a total of seven pressure cycles with a loading rate of 5 MPa/min (Figure 2). The effective pressure resulting from the confining and pore pressure was calculated following Terzaghi's effective pressure law (Terzaghi, 1925), assuming a linear pressure gradient (Hofmann et al., 2016):

$$p_e = p_c - p_p \tag{2}$$

with

$$p_p = p_{p,out} + \frac{p_{p,in} - p_{p,out}}{2} \tag{3}$$

In six of the cycles, the pore volume change was measured, while the sample permeability (Equation 1) was measured at several hydrostatic pressure levels in a seventh cycle. This ensured the stress-strain curves to

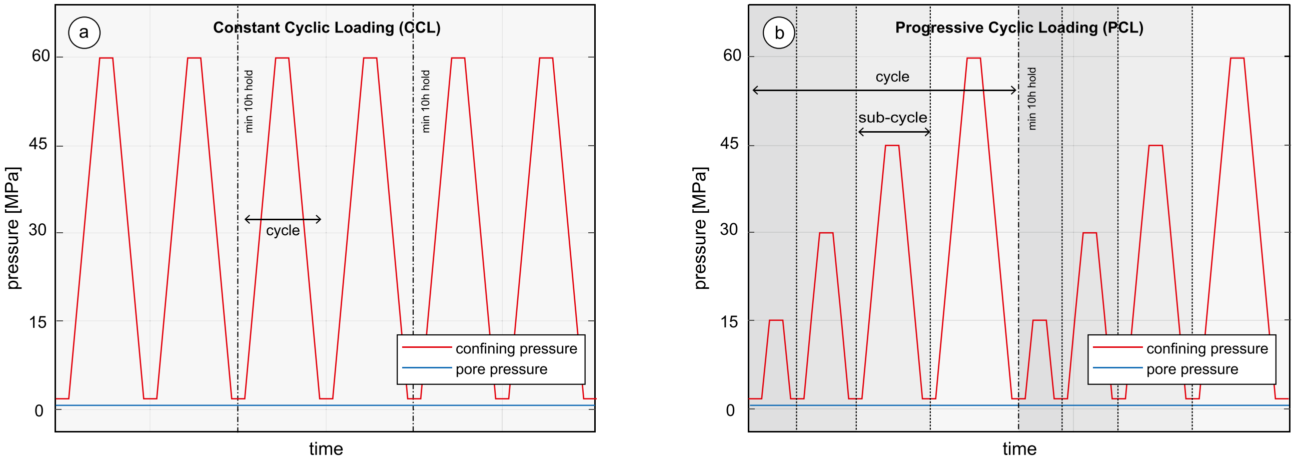

Figure 2. The constant cyclic loading (CCL) procedure (a) and the progressive cyclic loading (PCL) procedure (b).

be elastic. After preconditioning, samples were removed from the triaxial cell and dried in an oven at 50 C° for at least 24 hr.

The bulk volume change, V_{bulk} was calculated from the axial and circumferential strain, ϵ_a and ϵ_c, as well as the known initial volume, V_0:

$$\Delta V_{bulk} = (\epsilon_a + 2\epsilon_c) \cdot V_0 \tag{4}$$

2.3.2. Tensile Fracture Generation

To generate a single tensile fracture cutting through the diametrical axis of the sample, a modified Brazilian Disk test was used. The core was split over its entire length of 10 cm (Figure 1b). A low loading rate of 0.0003 mm/s was applied to avoid breakouts and to ensure a relatively planar fracture. The tensile strength, σ_{ts}, was calculated from the maximum measured load, F_{max}:

$$\sigma_{ts} = \frac{2F_{max}}{\pi dL} \tag{5}$$

After unloading the two sample halves were taken apart carefully (Figure 1c). Chipping of fragments from the surface could not be avoided completely.

2.3.3. Surface Scanning, Roughness and Aperture Analysis

After tensile fracture generation, both surfaces of the sample were analyzed with a 3D profilometer using the fringe pattern projection. The Keyence VR-3200 was used to measure the surface topography of all fracture surfaces with a point distance of 47 μm and an accuracy of 3 μm and 2 μm in the vertical and horizontal direction, respectively. Each surface was analyzed for its roughness exponent. Here, we apply a power spectral density method to obtain the scale-independent roughness exponent, H (Candela et al., 2012; Schmittbuhl, Vilotte, & Roux, 1995), based on the scaling relationship of $\delta x \rightarrow \lambda\delta x, \delta z \rightarrow \lambda^H \delta z$ (Meakin, 1998). Assuming the self-affinity of rock fracture surface (Schmittbuhl, Schmitt, & Scholz, 1995), the Fourier transform of all 1D profiles in the *x*-*y*-direction across the surface provides the power spectral density for the given spatial frequency domain in log-space. The slope of the spectrum then provides the roughness exponent in *x*-*y*-direction for every surface (Candela et al., 2012):

$$P(K) = Ck^{-1-2H} \tag{6}$$

where $P(k)$ is the Fourier power spectrum, k is the wave number, C is a pre-factor, and H is the roughness exponent. Since higher frequencies are over-represented in log-log-space, the mean spectra were re-sampled to 20 points (frequency) averaging the data in between for the linear fit. This way, all frequencies were evenly represented providing a better fit. The method was verified on a synthetic fault generated for two dimensional roughness exponents.

To obtain the aperture distribution of the top and bottom surface of one rock sample, the point cloud topography data of both surfaces were correlated. To calculate the aperture distribution of two independently scanned surfaces, both surfaces need to be matched. This was done by matching the best fitting principal planes of the bottom and top surface and applying a grid search algorithm. The surface data of both surfaces were interpolated on a grid with a point distance in *x*-*y*-direction of 0.05 mm. The top and bottom surfaces have the same orientation and shared the same grid. The fracture surfaces were displaced to an offset of 0.5 mm, as in the experiment. At each point across the x-y grid, the aperture (vertical distance) between the top and bottom surface was calculated to obtain the aperture distribution.

2.3.4. Procedures for the Fracture Flow Experiments

After generating and analyzing the fracture and its geometry the samples were prepared to perform the fracture flow experiments under the respective loading scenario (CCL and PCL). First, the two samples halves were placed together at a manual offset of 0.5 mm using perforated steel spacers at the opposite side of each sample half (Figure 1a). Any rotation of the two fracture planes can be ruled out due to the parallelism of the end cap and the spacer. The rigid shear offset of 0.5 mm was chosen based on three criteria: (a) larger than the grain size, (b) a comparable initial mean aperture for all three samples and (c) not too large to be able to measure the sample permeability (Equation 1) with our testing equipment (between $1 \cdot 10^{-18}$ m^2 and $1 \cdot 10^{-12}$ m^2). A brass stripe was used to cover the resulting holes caused by the spacers and the displaced fracture to avoid the heat-shrink tube to be punctuated (Figure 1d).

After the sample was installed in the triaxial cell, the confining pressure was increased to 2 MPa with a loading rate of 0.5 MPa/min. The fractured sample was then saturated for 24 h under vacuum conditions with a constant pore fluid pressure of 0.2 MPa. After the saturation, a constant inflow rate of 2.5–10 ml/min was applied from one side of the sample, while the outflow pressure was kept constant at 0.2 MPa, resulting in an effective pressure according to Equation 2.

The sample permeability was measured over the entire duration of the experiment. We assumed that measured flow rate is the sum of the individual flow rates through the matrix and through the fracture ($A_s k_s = A_m k_m + A_f k_f$). The matrix permeability, k_m, is assumed negligible comparing it to the fracture permeability, k_f. With the approximation of a rectangular shape of the fracture inflow surface ($A_f = 2ar$), we calculated the hydraulic aperture, a_h (Hofmann et al., 2016):

$$a_h = \sqrt[3]{6\pi k_s r} \tag{7}$$

Here, a_h is the hydraulic fracture aperture, k_s is the measured sample permeability, and r is the sample radius. From the hydraulic aperture we then calculated the fracture permeability, k_f, using the cubic law (Witherspoon et al., 1980):

$$k_f = \frac{a_h^2}{12} \tag{8}$$

Permeability errors were marginal and can hardly be quantified. The main error source was the frictional pressure losses within the capillary tubes connecting the fluid pumps and the sample, potentially leading to slight pressure changes. A second error source was the accuracy of the differential pressure transducer with an absolute error of 1% of the pressure range (1 MPa), which corresponds to only 1 kPa.

A circumferential LVDT extensometer chain was attached to the center of the sample to measure the bulk strain of matrix and fracture, ϵ_c. To remove the non-elastic strain from the total strain signal, we subtracted the fitted elastic strain of the intact rock sample, $\epsilon_{c,el}$, during the last loading and unloading cycle of the preconditioning. That way we obtained the strain of the fracture:

$$\epsilon_{c,frac} = \epsilon_c - \epsilon_{c,el} \tag{9}$$

The mechanical fracture aperture, a_m, was calculated from the sample diameter, d, and the corrected fracture strain, $\epsilon_{c,frac}$:

$$a_m = \epsilon_{c,frac} \cdot \frac{\pi d}{2} \tag{10}$$

The fracture specific stiffness, κ, was defined as the ratio of the increment of stress to the increment of displacement caused by the deformation of the void space in the fracture. The fracture stiffness, κ, was calculated from the change in fracture closure, $\Delta a_m = a_m(n+1) - a_m(n)$, per increment effective pressure increase, $p_e(n)$ averaged over an interval of 720 s (6 MPa):

$$\kappa = \frac{p_e(n+1) - p_e(n)}{a_m(n+1) - a_m(n)} \tag{11}$$

The interval of averaging only affects the smoothness of the signal to be able to better illustrate the stiffness evolution with changes in stress. Shorter intervals lead to noisy data while longer intervals lead to smoother data.

2.3.5. Constant Cyclic Loading (CCL) Experiment

The CCL experiment at hydrostatic conditions was performed according to Figure 2a, using sample SBT6-BE-04-03. The confining pressure was increased from 2 to 60 MPa at a constant loading rate of 0.5 MPa/min. At 60 MPa, the confining pressure was held for 20 min before unloading was started at the same rate as during loading. This process was repeated six times to obtain the fracture closure curves for a constant loading procedure with the same peak stress. After two cycles, the system was held at a constant low-level load for about 12 hr.

2.3.6. Progressive Cyclic Loading (PCL) Experiments

The PCL experiments at hydrostatic conditions were performed according to Figure 2b, using samples SBT6-BE-04-09 and SBT6-BE-04-10. In this procedure, we distinguished between pressure cycles and pressure sub-cycles. The sub-cycles describe the stepwise increase of hydrostatic confining pressure from 2 to 15, 30, 45, and 60 MPa. One sub-cycle was therefore the increase from 2 to the respective stress level (15, 30, 45, and 60 MPa) and the decrease or unloading from the respective stress level to 2 MPa. The confining pressure was held for 20 min before unloading was started at the same rate as during loading. That way, the effective pressure was increased by an additional 15 MPa over the previous pressure level to identify potential changes in the fracture closure or opening behavior when exceeding the previous stress level. This PCL was repeated two times, that is, two complete cycles, with a hold phase of about 10 hr between the two. The loading rate for the confining pressure was 0.5 MPa/min for loading and unloading.

At the end of the experiments, the samples were removed from the cell and dried at 50 C for at least 24 hr. The fracture surfaces were scanned and analyzed as described in Section 2.3.3.

3. Experimental Results

3.1. Sample Volume and Permeability of the Intact Rock

Based on the bulk volume change (Equation 4), the plastic and elastic sample deformation was monitored during six loading cycles up to 65 MPa (Figures 3a–3c). Most of the irreversible plastic deformation was found in the first loading cycle (Figures 3a–3c). After six pressure cycles, no more significant bulk strain changes suggested fully elastic sample deformation. The total volume loss was about 0.27 cm^3 measured by the volumetric strain and 0.39 cm^3 measured by the pore volume change. This corresponded to about 0.1% of the initial porosity of 5%–6%. The seventh loading cycle is not shown here, because the fluid pressure in the sample was higher during the permeability measurements.

In the seventh loading cycle, the intact rock permeability (Equation 1) was measured at four to five pressure levels during loading and unloading (Figure 3d). The sample permeability, k_s at 2 MPa was reduced from about 1 to $3 \cdot 10^{-15}$ m^2 before pre-conditioning down to $5 \cdot 10^{-18}$ m^2–$1 \cdot 10^{-17}$ m^2 after pre-conditioning. This corresponds to a difference of more than two orders of magnitude. The largest incremental change in permeability was found during the first 15 MPa of confining pressure, while the change becomes smaller after 40 MPa. At effective pressures larger than 40 MPa the permeability was about $1 \cdot 10^{-19}$ m^2, which was the lower limit of measurable permeability with our machine. The permeability of all measured samples showed a similar behavior. During loading, the permeability was overall higher compared to unloading and the change in permeability was always reversible after pre-conditioning.

3.2. Tensile Fracture Generation

The tensile strength, TS, calculated from Equation 5, for the three samples SBT6-BE-04-03, 09, and 10 was 5.4, 4.0, and 5.5 MPa, respectively. The mode I fracture toughness, K_{Ic}, was calculated after Guo et al. (1993)

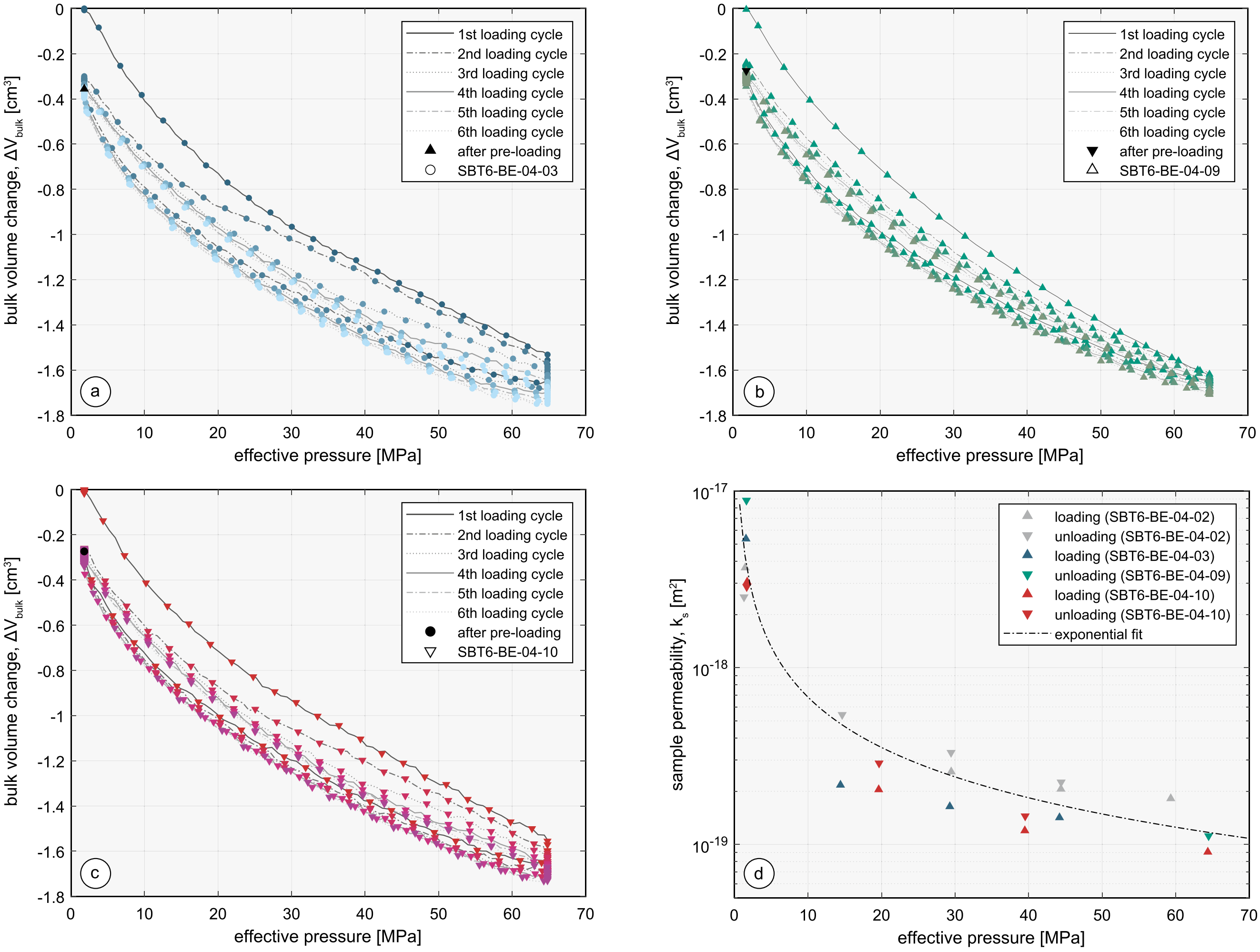

Figure 3. The bulk volume change during pre-conditioning (a, b, c) and the pressure-dependent permeability of the intact rock sample (d).

and corresponded to 0.78, 0.63, and 0.82 MPa·m$^{1/2}$, respectively. The sample halves were taken apart, loose fragments were carefully removed and possible breakouts at the corners were filled with an Araldite-sand mixture. This was done to avoid inward bulging and rupture of the heat-shrink tube during loading. However, it did not lead to additional contact-area between the opposing fracture surfaces and had thus no impact on the strength or stiffness of the fracture.

3.3. Constant Cyclic Loading (CCL) Experiment

3.3.1. Fracture Permeability and Aperture During CCL

Comparing the initial sample permeability after pre-conditioning (Figure 3b), to the initial sample permeability containing a fracture at 2 MPa effective pressure (Equation 1), we found an increase from $5.4 \cdot 10^{-18}$ m^2 to about $6.0 \cdot 10^{-13}$ m^2. In the following, we will refer permeability to the fracture permeability calculated following Equation 8. During the first loading cycle from 2 to 60 MPa of the confining pressure, the permeability reduced from $3.5 \cdot 10^{-10}$ m^2 to $2.9 \cdot 10^{-12}$ m^2 (Figure 4a). While the permeability changes were only minor during the first 20 MPa, the largest permeability decrease was observed above a confining pressure of 20 MPa. During the hold phase, the permeability reduced slightly but reached an almost constant level within 20 min (Figure 4b). The permeability recovery when reducing the effective pressure was slower than the permeability loss during the effective pressure increase. When reaching 2 MPa, the permeability loss was more than one order of magnitude with a permeability of about $2 \cdot 10^{-11}$ m^2 at the end of the first cycle. During the second loading cycle, the incremental permeability decrease was larger at lower stress,

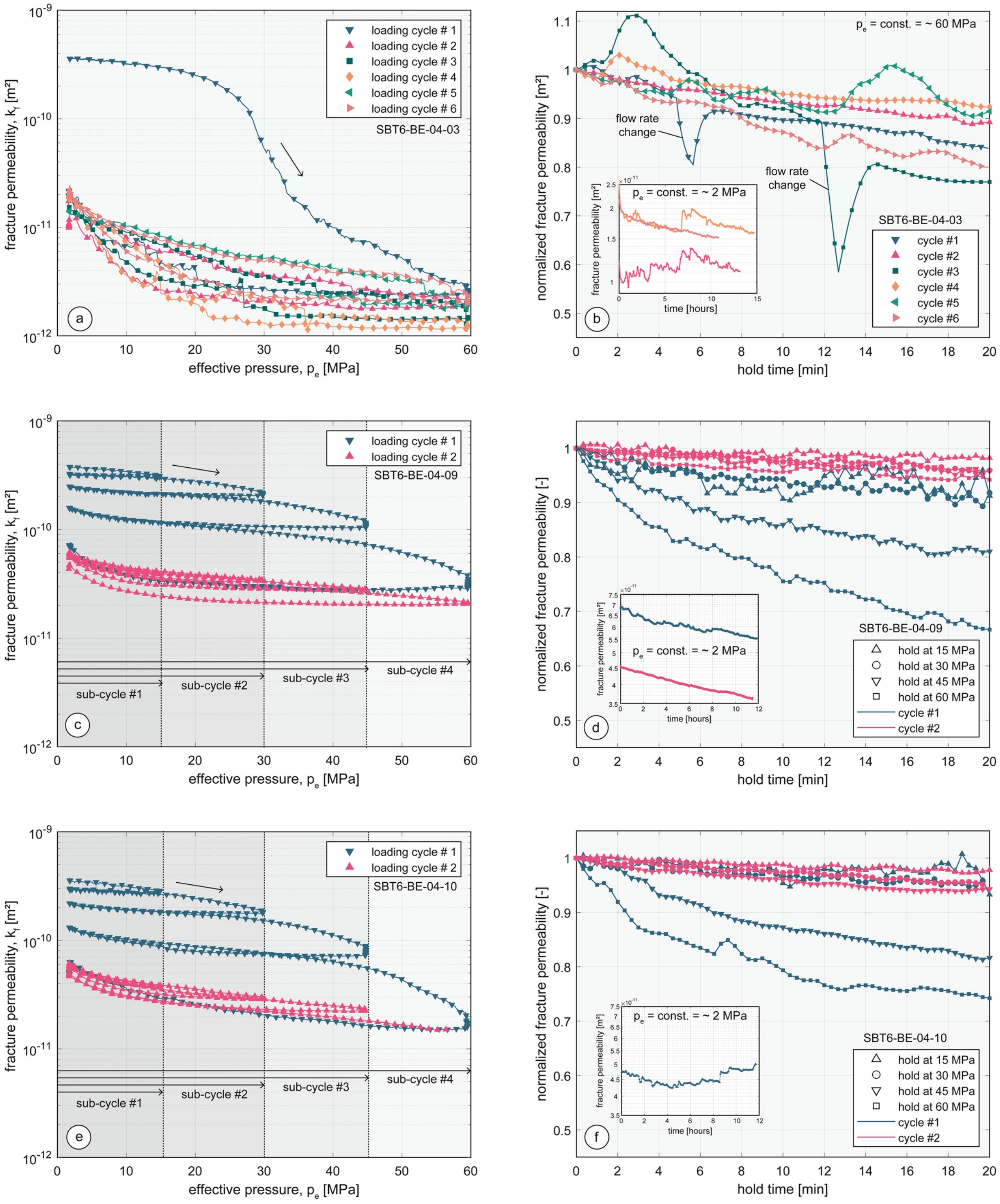

Figure 4. Fracture permeability of the constant cyclic loading (CCL) experiment and the hold phases (a, b), as well as the progressive cyclic loading (PCL) experiments and the hold phases (b, c, d, e). Permeability was normalized to the first value of permeability during the hold phase.

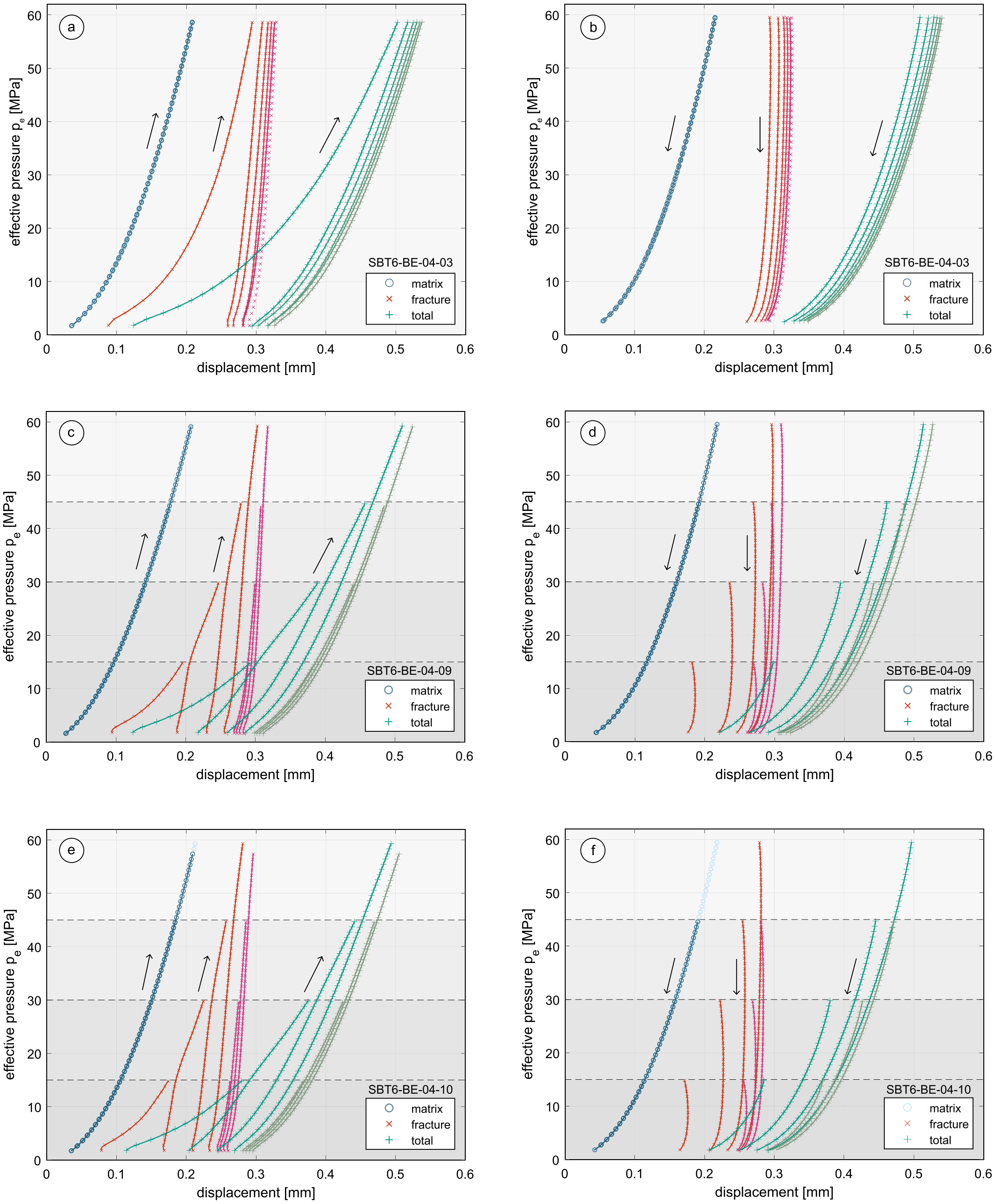

Figure 5. The total fracture closure during constant cyclic loading (CCL) and progressive cyclic loading (PCL) experiments during loading (a, c, e) and unloading (b, d, e).

while only minor permeability losses were observed at an effective pressure above 30 MPa. The minimum permeability at 60 MPa in the second cycle was $1.9 \cdot 10^{-12}$ m^2. In the following cycles, the trend of the second loading cycle was maintained and a reversible fracture permeability was observed. There was almost no permeability reduction during the overnight hold phases (Figure 4b, inset). Smaller and short-term peaks in permeability were related to changes in the flow rate during loading and unloading.

The maximum elastic matrix deformation measured with the axial extensometers was no more than 0.14 mm at 60 MPa (Figure 5a). Subtracting this from the total radial deformation of about 0.53 mm after the first loading cycle, the actual fracture closure was roughly 75% of the total measured deformation resulting from six cycles. While the matrix compaction was fully elastic within the six loading cycles, the residual

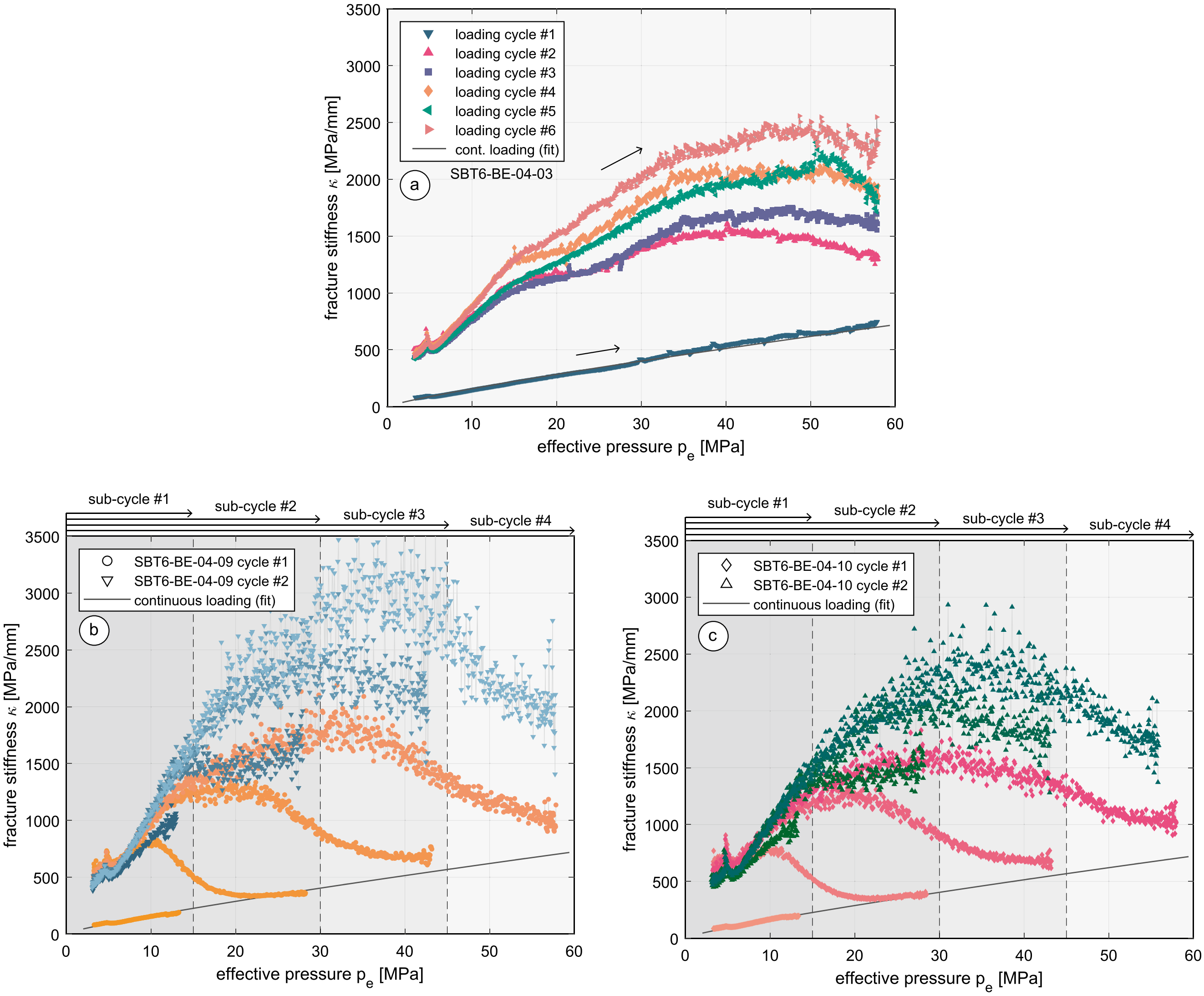

Figure 6. The fracture stiffness evolution during constant cyclic loading (CCL) and progressive cyclic loading (PCL) experiments during loading.

fracture closure was 0.28 mm after the first loading cycle at 2 MPa. The following cycles showed further fracture closure by up to 0.37 mm. The incremental fracture closure with increasing stress was rather linear at effective pressures larger than 20 MPa. During unloading, the fracture remained closed until about 10–15 MPa (Figure 5b). This was similar to the permeability data, which shows a nearly constant permeability until about 10–15 MPa.

3.3.2. Fracture Stiffness Evolution During CCL

The fracture stiffness was calculated following Equation 11 at intervals of 720 s. This was done to reduce the noise related to the sensors only with impacts on the signal quality of the fracture stiffness. The results were separated to first calculate the fracture stiffness during the successive loading cycles (Figure 6a). In the first loading cycle, the fracture stiffness increased linearly from about 80 MPa/mm to about 750 MPa/mm at 60 MPa. The 2^{nd}–6^{th} loading cycles showed a nonlinear but reversible fracture stiffness evolution. Only minor increases with progressive loading cycles were found, smaller than noise measurements. This reversible fracture stiffness from the second loading cycle was higher compared to the first loading cycle, with values between 450 MPa/mm at 2 MPa and up to 2,300 MPa/mm at 60 MPa. The peak stiffness was reached at about 40–50 MPa with a slight decrease toward the final stress level.

Table 2
Fracture Stiffness Results During the Respective Loading Cycles

Stress-path per cycle (MPa)	Cycle number[a]	Stiffness range (MPa/mm)	Stiffness trend
SBT6-BE-04-03 (CCL)			
(2–60)	1	80–750	Linear
(2–60)	2–6	450–2,300	Nonlinear
SBT6-BE-04-09 (PCL)			
(2-15-2-30-2-45-2-60)	1	80–1,000	Linear to nonlinear[b]
(2-15-2-30-2-45-2-60)	2	500–2,000	Nonlinear
SBT6-BE-04-10 (PCL)			
(2-15-2-30-2-45-2-60)	1	80–1,000	Linear to nonlinear[b]
(2-15-2-30-2-45-2-60)	2	500–1,700	Nonlinear

[a] One cycle is one repetition of the stress path per cycle. [b] Transition when exceeding the previous stress level during each sub-cycle.

During unloading, the fracture displacement (Figure 5a) was almost constant, that is, the fracture remained closed. Therefore, fracture stiffness was undetermined until a stress of about 10–15 MPa.

3.4. Progressive Cyclic Loading (PCL) Experiments

3.4.1. Permeability and Aperture During PCL

In the following, we refer to loading sub-cycles as the pressure change from 2 to 15 MPa, 2 to 30 MPa, 2 to 45 MPa, and 2 to 60 MPa, as well as a full loading cycle, which is a complete set of the four sub-cycles (Figure 2). We performed a total of two complete loading cycles for samples SBT6-BE-04-09 and 10.

The fracture permeability was first measured at 2 MPa confining pressure with values of about $3.7–3.8 \cdot 10^{-10}$ m^2 (Figures 4b and 4c). This was close to the highest permeability that can be measured in our testing device. The flow rate was set to a maximum of 10 ml/min to avoid turbulent flow conditions. Permeability reduced after every loading cycle, with a larger reduction with increasing pressure in the respective sub-cycle. The permeability reductions after each sub-cycle during the first cycle to 15, 30, 45, and 60 MPa correspond to a factor of 1.2, 1.3, 1.6, and 2.2 compared to the initial permeability. During re-loading, the permeability follows the same permeability trend as during unloading up to 20 MPa. At stresses higher than 20 MPa, the permeability was lower during loading compared to unloading. After the first loading cycle, a permeability loss by a factor of 5.2 was measured for both samples. This corresponds to about $3.5–3.7 \cdot 10^{-10}$ m^2 at the beginning and $0.5–0.7 \cdot 10^{-10}$ m^2 at the end of the first cycle. During the hold phases, a continuous reduction of permeability was observed at stresses above 30 MPa, with an increasing reduction at increasing stress levels (Figures 4d and 4f). In the second loading cycle, the permeability was almost reversible, following the trend during unloading up to about 45 MPa, a further reduction was found. The permeability reduction during the hold phases in the second cycle was minor compared to the initial loading cycle.

The elastic matrix deformation was roughly 30% of the bulk deformation measurement. Therefore, about 70% of the total deformation was related to fracture closure (Figures 5c and 5e). When re-loading the fracture, the aperture follows the unloading path until reaching the previous stress level. After that, the fracture closure was larger, meaning that the slope of the fracture closure versus the effective pressure curve was shallower. This trend was similar in all sub-cycles up to 60 MPa. The total closure in sample SBT6-BE-04-09 and 10 at the end of the second loading cycle was 0.37 and 0.35 mm. During unloading, the fracture remained closed until about 10 MPa (Figures 5d and 5f). This was similar to the permeability data, which shows a nearly constant permeability until about 10 MPa.

3.4.2. Fracture Stiffness Evolution During PCL

The fracture stiffness results during the respective sub-cycles are summarized in Table 2. Both PCL experiments (SBT6-BE-04-09 and 10) showed the same trend and magnitudes of fracture stiffness. The effective stress was increased from 2 to 15 MPa during the first sub-cycle. This resulted in a linear increase in fracture stiffness with increasing effective pressure from around 80 to about 190 MPa/mm (Figures 6b and 6c). During the 2^{nd} sub-cycle, the pressure was increased from 2 to 30 MPa. The fracture stiffness initially followed the nonlinear fracture stiffness curve of the 2^{nd} to the 6^{th} of the CCL experiment (SBT6-BE-04-03), starting from around 500 MPa/mm. Fractures stiffness decreased shortly before reaching the effective stress of 15 MPa. The curve returned back to the linear fracture stiffness curve of the first loading cycle of the CCL experiment. This resulted in a fracture stiffness of around 350–400 MPa/mm at 30 MPa for both samples. During the third sub-cycle, the stress was increased from 2 to 45 MPa. The fracture stiffness followed the nonlinear trend of the 2^{nd} to 6^{th} loading cycle of the CCL experiment, as well as the second sub-cycle recorded before that. Both samples kept following this trend exceeding a pressure of 15 MPa, but fracture stiffness started to decrease shortly before reaching the previous stress level of 30 MPa. Again, the fracture stiffness returned to the linear trend of the first loading cycle of the CCL experiment, reaching an end value of about

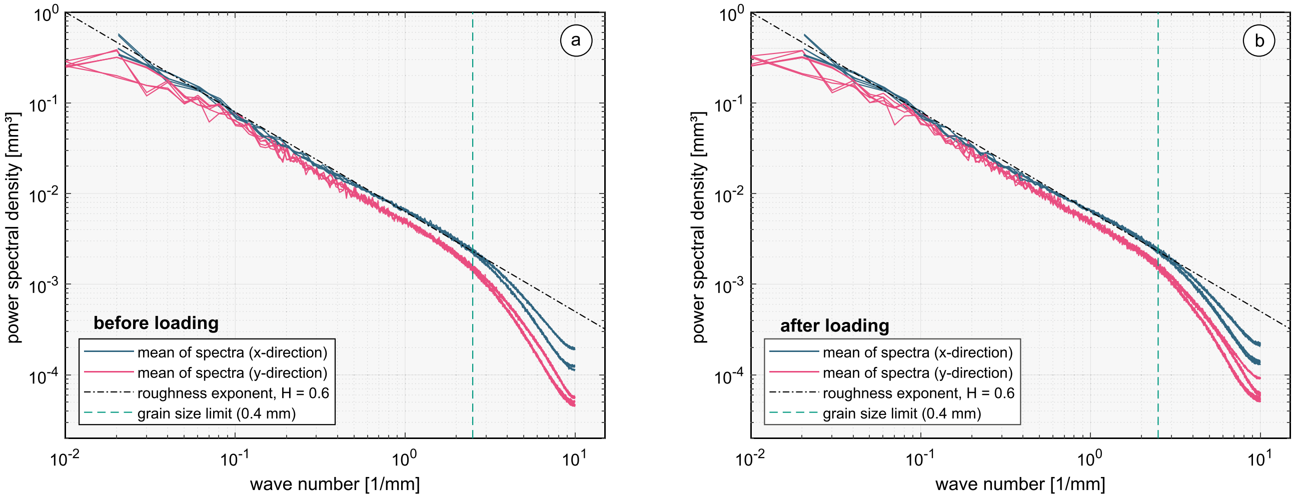

Figure 7. The direction-dependent roughness exponent of all fracture surfaces A and B before (a) and after (b) cyclic loading.

700 MPa/mm at 45 MPa. During the 4th and last sub-cycle, the pressure was increased from 2 to 60 MPa. The fracture stiffness was similar to that of the 2nd–6th loading cycle of the CCL experiment, as well as the 1st and 2nd sub-cycle of the PCL experiment. The fracture stiffness deviated from the nonlinear fracture stiffness shortly before reaching 45 MPa, but the reduction was smaller compared to the clear drop of the second sub-cycle before 15 MPa. The fracture stiffness almost reached the end value of about 1,000 MPa/mm of the first loading cycle of the CCL experiment at 60 MPa. At stresses larger than 50 MPa we found less changes in fracture stiffness with increasing stress. The smaller reduction in stiffness when reaching the previous stress level of 45 MPa indicated less fracture closure with increasing stress. The four sub-cycles were repeated in a second cycle of the PCL experiments, increasing pressure from 2 to 15, 30, 45, and 60 MPa, respectively. During all subsequent loading sub-cycles, the fracture stiffness followed a similar nonlinear trend as during the 2nd–6th loading cycle of the CCL experiment.

Similar to the CCL experiment, the fracture displacement (Figures 5b and 5c) was almost constant during unloading until about 10 MPa, resulting in an undetermined fracture stiffness.

3.5. Fracture Geometry Before and After Cyclic Loading

3.5.1. Fracture Roughness Exponent

The roughness exponent was determined using the power spectral density approach as explained in Section 2.3.3. Assuming that the tensile fracturing in sandstones was exclusively intergranular, the higher frequencies reflect the surface roughness of the grains (Boffa et al., 1998). Those frequencies led to deviations in the power spectrum. They were suppressed by a frequency cutoff for length scales that are two times the grain size, that is, two times 0.2 mm. The resulting cutoff frequency additionally marks a break in the slope and a deviation from a linear trend in log-space. Figure 7 shows the power spectrum for the surfaces before and after the flow-through experiments in *x*-*y*-directions. The slope of the fitted trend eventually leads to the roughness exponent (Equation 6).

Table 3
Fracture Roughness Exponents

	x-direction		*y*-direction	
Surface ID	Before	After	Before	After
SBT6-BE-04-03-A (CCL)	0.55	0.55	0.58	0.58
SBT6-BE-04-03-B (CCL)	0.60	0.56	0.57	0.60
SBT6-BE-04-09-A (PCL)	0.57	0.57	0.58	0.54
SBT6-BE-04-09-B (PCL)	0.58	0.57	0.59	0.56
SBT6-BE-04-10-A (PCL)	0.58	0.58	0.60	0.61
SBT6-BE-04-10-B (PCL)	0.59	0.59	0.61	0.61

The power spectra indicate a similar roughness exponent for all surfaces independent of the direction (Table 3). We found a mean of 0.58 (±0.02) in *x*-direction and 0.57 (±0.02) in *y*-direction (shear direction) before the experiment. These values are in agreement with roughness exponents of around 0.5–0.6 for sandstones that are commonly slightly lower than the 0.8 found for most other rock types (Boffa et al., 1998). After the cyclic loading experiment, the surface topography was obtained a second time in the same orientation as before. The post-experimental mean values for

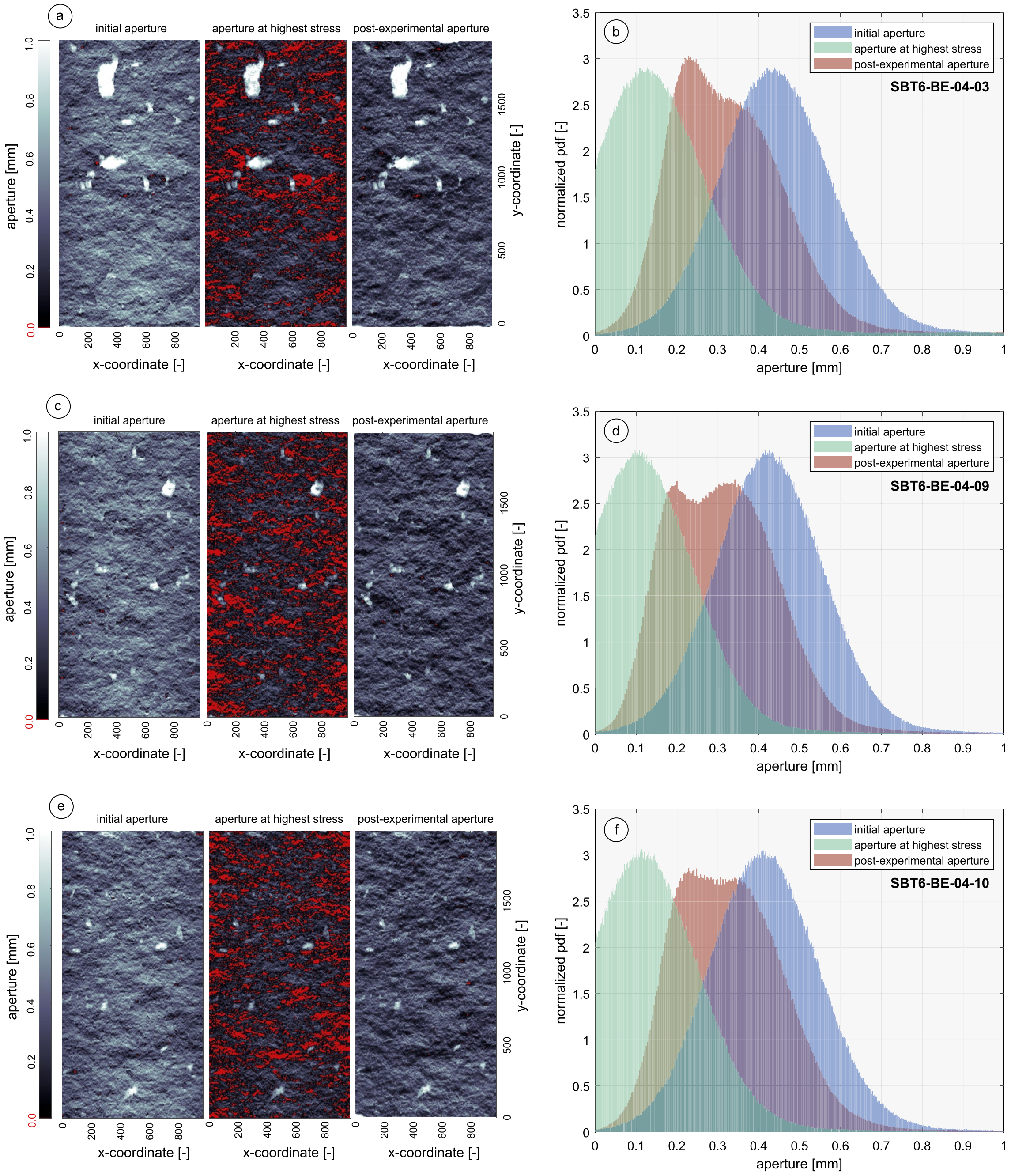

Figure 8. Fracture aperture before and after cyclic loading, as well as the aperture distribution before the experiments, at the highest stress, and after the experiment.

the roughness exponent in the *x*-*y*-direction were 0.57 (±0.01) and 0.58 (±0.03), respectively. This indicated no distinct change in the scaling properties of the surface roughness due to the cyclic loading.

3.5.2. Fracture Aperture Distribution and Contact-Area Ratio

From the surface topography from each fracture surface, we calculated the aperture distribution by matching the top and bottom surfaces as explained in Section 2.3.3 (Figures 8a, 8c and 8e; left). The aperture, a, was taken as the distance between each point across a *x*-*y*-grid (point distance 0.05 mm). This was done to calculate the initial aperture distribution of every sample. We considered this aperture distribution as the initial aperture, a_{ini}, at zero stress. With the assumption of two interpenetrating surfaces under normal load,

Table 4
Mean Fracture Apertures and Contact-Area Ratio

Sample ID	$\overline{a}_{ini}$ (mm)	Δa_{max} (mm)	$\overline{a}_{min}$ (mm)	$R_{c,max}$ (−)	$\overline{a}_{post}$ (mm)
SBT6-BE-04-03 (CCL)	0.46	−0.310	0.15	0.16 ± 0.05	0.34
SBT6-BE-04-09 (PCL)	0.43	−0.318	0.11	0.20 ± 0.05	0.31
SBT6-BE-04-10 (PCL)	0.42	−0.296[a]	0.12	0.18 ± 0.05	0.33

Note. $\overline{a}_{ini}$, initial mean aperture; Δa_{max}, maximum measured closure (at 60 MPa). $\overline{a}_{min}$, minimum mean aperture; $R_{c,max}$, maximum contact-area ratio. $\overline{a}_{post}$, post mean aperture.

[a] Data until about 58 MPa.

that is, geometrically overlapping regions are assumed to be in contact without deformation (the "overlap" model; Pei et al., 2005), we calculated the resulting evolution of contact-area ratio, R_c. It is commonly defined as the ratio of the surface area in contact, A_c and the total surface area, A_t:

$$R_c = \frac{A_c}{A_t} \tag{12}$$

Considering only one contact point at zero stress would lead to an overestimation of the mean aperture when small fragments protrude from the fracture surface. Similar to Wang and Cardenas (2016), we defined a threshold to shift the normal distribution to the left and reduce the aperture. The two fracture surfaces were brought into contact at an initial contact-area ratio, R_c, of 0.1%. Furthermore, we consider the contact-area (zero aperture) as a discontinuity (delta function) in the aperture distribution (Pyrak-Nolte & Morris, 2000) and excluded these values when calculating the mean aperture.

The initial aperture distribution of all samples showed a similar normal distribution of aperture (Figures 8b, 8d and 8e), with mean apertures of 0.46, 0.43, and 0.42 mm (Table 4). The larger local apertures of sample SBT6-BE-04-03 were caused by small fragments removed during the tensile fracturing process. The maximum fracture normal closure during loading was obtained from the LVDT extensometer and calculated according to Equation 10. The maximum measured fracture closure at about 60 MPa in the second cycle, Δa_{max}, was subtracted from the initial aperture distribution, a_{ini}. Although this simplifies the process of two surfaces coming into contact, it allowed for an estimation of the mean fracture aperture at the largest stress. The maximum fracture closure, Δa_{max}, for samples SBT6-BE-04-03, 09, and 10 were −0.310, −0.318, and −0.296 mm. The data of sample SBT6-BE-04-09 was only recorded up to about 58 MPa in this cycle. The resulting minimum mean apertures at highest effective stress in the second loading cycle, $\overline{a}_{min}$, corresponded to 0.15, 0.11, and 0.12 mm, respectively (Table 4). There was a slight trend in the data indicating that the higher the initial mean aperture, the higher the fracture closure at the end of the second complete loading cycle. The maximum contact-area ratio, $R_{c,max}$, at the maximum effective stress at the end of the second loading cycle, was between 16% and 20% for all samples (Table 4). The contact-area, that is, zero apertures were marked in red in Figures 8a, 8c and 8e (center). Here, we observed that the layering of the sample (perpendicular to the shear-direction), was visible in the contact-area distribution leading to "contact bands" along the bedding. This possibly resulted in smaller necks for fluid flow at large stress. The contact points were predominantly distributed along the edges of the sample indicating a generally concave shape of the fracture surface. This might result from a combination of the tensile fracture generation during diametrical loading conditions deforming the fracture surface and the finite size effect of the samples.

After the experiment, the mean aperture at no confining pressure was between 0.31 and 0.34 mm for all samples, which corresponds to a total permanent aperture reduction of about 0.09–0.12 mm (Figures 9a, 9c and 9e; right). A kink at the peak of the normal distribution in the post-experimental aperture distribution indicates changes in the fracture topography (Figures 9b, 9d and 9f). Due to the anisotropic deformation, caused by one-sided "contact bands" perpendicular to shearing, we observe a cutoff of the mean aperture. This process was possibly more pronounced in the CCL sample compared to the PCL samples. It was not possible to relate the statistical aperture distribution to differences in measured permeability. Permeability not only relies on the aperture distribution but also on the spatial correlations in the aperture (self-affine property). For the same aperture distribution, with or without spatial correlations, the fracture will have a different permeability.

The mean aperture with increasing shear offset before and after the experiment was compared and is shown in Figure 9a. Here we found a mechanical imprint after cyclic loading, meaning that the mean aperture at zero offset was higher and reduced toward the given shear offset applied during the experiment (0.5 mm). The lowest mean aperture was found at a shear offset of 0.35 mm. At a shear offset above 1 mm, the mean apertures after the experiment are similar to those before the experiment. Although no change in roughness above grain scale was found, a change in fracture topography was visual when comparing the mean aperture with increasing shear displacement.

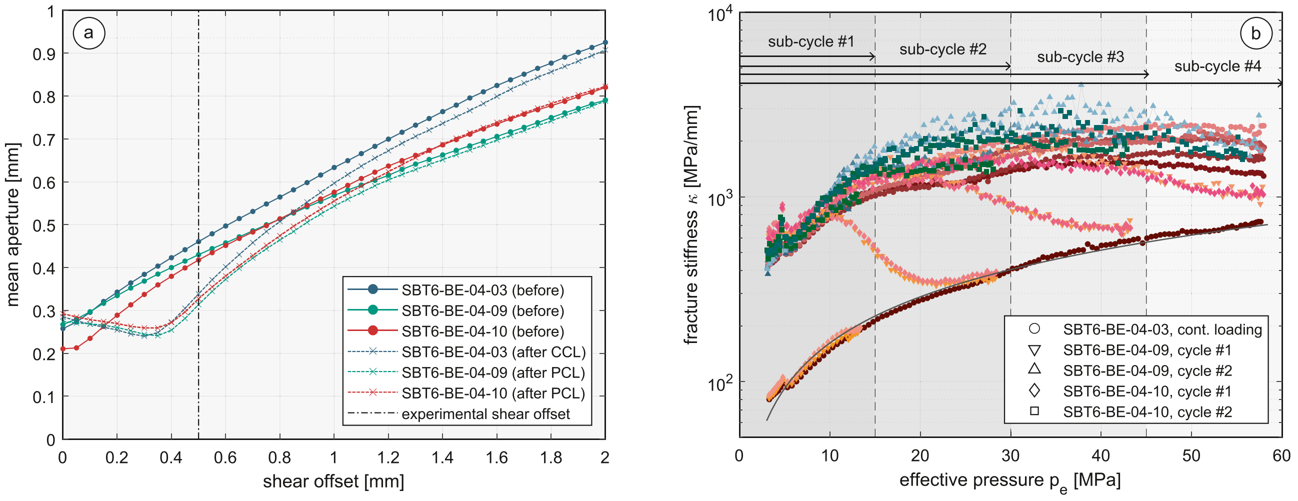

Figure 9. The fracture mean aperture versus the shear offset (a) and summary of fracture stiffness evolution during constant cyclic loading (CCL) and progressive cyclic loading (PCL) (b).

4. Discussion

4.1. Fracture Stiffness Evolution and the Stress Memory Effect

In this section, we discuss the evolution of fracture stiffness with increasing stress. We address the debate about the linearity of fracture stiffness with increasing effective pressure, as well as the hysteresis effect during loading and unloading. We then relate our findings to a possible "memory effect" of fracture stiffness during the PCL experiments.

The loading and unloading path of fracture closure during loading shows a hysteresis effect (Figure 5). This is well known (Bandis et al., 1983; Brown & Scholz, 1986; Cook, 1992; Pyrak-Nolte, 1987; Skurtveit et al., 2020; Thörn et al., 2015; Yoshioka, 1994; Zou et al., 2020). During cyclic loading, hysteresis decreases and consequently the displacement between cycles decreases (Bandis et al., 1983; Brown & Scholz, 1986; Pyrak-Nolte, 1987). We see the same behavior in our CCL experiments. During unloading, the fracture remains closed at higher stress and opens only at a stress below 10 MPa, even though applying the same pressure rate of 0.5 MPa/min. This leads to larger and permanent fracture closure magnitudes, especially during and after the first loading cycle.

The fracture stiffness magnitudes were similar for all three experiments (Figure 6). We assume that the data of all three experiments are repeatable and that the experimental workflow and boundary conditions led to consistent data. However, small deviations in fracture geometry between the samples can cause large deviations in fracture stiffness (Pyrak-Nolte & Morris, 2000). The measured fracture normal closure is largely dependent on the position along the sample. Furthermore, the measured values are dependent on local variations caused by local aperture and contact-area variations (Cook, 1992; Marache et al., 2008). Our calculated stiffness values were in the range of 80–3,000 MPa/mm for a sample scale of 100 mm, similar to experiments at the same effective pressure ranges with sandstone reported by Y. Chen et al. (2017) and Skurtveit et al. (2020).

From the CCL experiments, we found a stress-path-dependent fracture stiffness with a linear trend during the initial loading phase and a nonlinear but reversible trend for all subsequent loading cycles (Figure 6a). Previous studies reported contrasting results: while most authors describe a linear relationship of stiffness and stress with different slopes for different stress magnitudes (Akarapu et al., 2011; Bandis et al., 1983; Cook, 1992; Persson, 2007; Pyrak-Nolte, 1996; Wang & Cardenas, 2016; Zou et al., 2020), some reported a partly nonlinear increase of fracture stiffness (Cook, 1992; Raven & Gale, 1985; Pyrak-Nolte, 1987; Pyrak-Nolte & Morris, 2000). From our data, we see that linearity or nonlinearity of fracture stiffness is not trivial, but depends on the stress history of a fracture. During initial loading, the stiffness trend with increasing stress is linear up to at least 60 MPa. The linear behavior can be caused by multiple rheologies, such as elastic, plastic, and elasto-plastic (Greenwood & Williamson, 1966; Kling et al., 2018; Pei et al., 2005; Persson, 2006; Zou et al., 2020). At higher stresses and depending on the rock type, roughness and host rock properties, a change in slope at a certain stress level during initial loading might be possible (Wang & Cardenas, 2016). This linear behavior is not reversible when re-loading the sample within the same range of stress. During these subsequent loading cycles, the system becomes nonlinear. The non-reversible behavior clearly indicates plastic effects. The nonlinear fracture stiffness trend is characterized by an initially steep increase at effective pressures up to 10 MPa and being reduced before reaching the previous maximum stress level for sandstones. Several repeated loading cycles lead to a slight increase in the nonlinear stiffness trend (Figure 6a). Therefore, an additional contribution due to the plastic component during repeated loading cannot be excluded. Since the maximum stress in both experimental scenarios (CCL and PCL) was 60 MPa, we see a slight reduction of fracture stiffness toward that maximum. Further increase in stress beyond 60 MPa might lead to a return of stiffness toward the linear trend of the first loading cycle. It is not clear at what stress the stiffness might lead a limiting value. The initial fracture stiffness during unloading, that is, the constant fracture closure, indicates a permanent aperture reduction with only a minor recovery at stress levels below 10 MPa (hysteresis effect).

When exceeding the previous stress level during re-loading, however, the nonlinear fracture stiffness trend returns to a linear trend (Figures 6c and 6e). This behavior was observed in our PCL experiments. During unloading the fracture remains closed. When exceeding the previous stress, the change from nonlinear to linear fracture stiffness behavior can be repeated. We conclude, this effect is similar to the "Kaiser Effect" (e.g., Kaiser, 1953) and reveals a stress-memory effect of fracture stiffness during PCL. Figure 9b summarizes the fracture stiffness evolution of the CCL and PCL experiments for stresses of up to 60 MPa. It is not clear whether fracture stiffness approaches a limiting value independent of the number of cycles at higher stresses. The turning point from nonlinear to linear was visible already before the previous peak load is reached. This is similar to the classic "Kaiser Effect" in uniaxially loading tests with intact rock while monitoring acoustic emissions (Lavrov, 2005). Additionally, the fracture stiffness reaches its initial path with some delay.

Lavrov (2005) argued that the stress-memory effect may decay in the course of time, that is, when the time interval between successive loading cycles is increased. Whether the stress-memory effect of fracture stiffness decays over time cannot be seen from our data. This is because the time frame of the experiments was too short. We could show that the stress-memory effect is measurable using saturated samples. Experiments by Lavrov (2003) showed that a change in moisture is critical using acoustic emission when trying to detect the "Kaiser Effect."

4.2. Relationship of Mechanical and Hydraulic Properties

The fracture stiffness describes the amount of fracture closure with increasing normal stress and therefore directly affects the hydraulic properties of fractures.

Pyrak-Nolte and Morris (2000) described that fluid flow and fracture-specific stiffness are implicitly related since both depend on the size and spatial distribution of aperture and contact-area, or more generally, the fracture geometry. Additionally, stiffness is not only dependent on stress magnitude, since all of the fractures they tested appeared to behave differently, such that any interrelationship among the fracture properties was obscured. They related this to the formation of new contact area as a direct function of the aperture distribution affecting the fracture normal closure. Albeit no relation to the stress magnitude was found, it was concluded that stiffness is dependent on the stress path. Our data support this assumption, while we also observed similar stiffness values at similar stress states. This is possibly due to the accurate sample selection from one block and the resulting compatibility of the three experiments. Contrary, the variety of trends shown by Pyrak-Nolte and Morris (2000) can be caused by a larger variety in fracture geometries of natural fractures. Attempts to normalize the relation of fracture stiffness and permeability were made by Pyrak-Nolte and Nolte (2016) based on numerical simulations. Unfortunately, the required scale-dependent fracture stiffness and permeability cannot be derived from the bulk measurements we obtained in the laboratory.

The initial large decrease in permeability can be explained by a change of flow regime from sheet-like to channelized flow. In this "percolation regime," the contact-area remains unchanged (Cook, 1992; Pyrak-Nolte, 1987; Zimmerman, 2008) and a residual fracture permeability is observed (Milsch et al., 2016). It implies that permeability becomes increasingly independent of stress (Pyrak-Nolte, 1987; Petrovitch et al., 2013). PCL leads to a higher residual fracture permeability compared to CCL. This highlights the fact that permeability is also a stress-path-dependent property for this type of rock.

Both, CCL and PCL lead to hysteresis effects in permeability, especially between the first and second loading cycles. We could show that after the first complete loading cycle up to 60 MPa, permeability was permanently reduced, that is, the fracture did not fully re-open. In all following loading cycles, permeability also showed hysteresis effects. Permeability was always reduced to about the same value at the lowest applied normal load. Such a behavior was shown already (e.g., Z. Chen et al., 2000; Hofmann et al., 2016; Kluge, Blöcher, et al., 2017; Milsch et al., 2016; Pyrak-Nolte & Morris, 2000; Watanabe et al., 2009). Applying a PCL procedure shows a surprising behavior. When reloading the fracture, permeability reduces less than during initial loading and permeability starts to decrease more when the previous peak load is exceeded, as expected. When comparing the total permeability reduction after the second cycle, progressive loading leads to less permeability reduction compared to constant loading conditions. The main difference in permeability evolution was found at the effective pressure of 20 MPa. We believe that permeability is affected by the allocation of crushed asperities. During CCL, the crushed material remains relatively in place, blocking potential fluid pathways and therefore continuously reduces permeability. During the PCL, the stress is released after reaching a certain stress level before increasing the stress further. That way, fines are potentially flushed out of the sample or allocated to larger fracture void spaces with low flow velocities when reducing the load to a minimum. Since the aperture is self-affine with an roughness exponent of about 0.6 (it is even stronger for $H = 0.8$), open spaces are extending on larger scales than for a random surface with no self-affine properties (negative H), and accordingly channeling is stronger. This possibly leads to a higher permeability compared to the continuous loading process. This can only be shown by analyzing the effluent or analyzing the fracture morphology before and after the experiments and therefore requires further studies. The resolution of the surface scans was insufficient to detect their possible changes.

The stiffening effect by progressive loading can be explained by three causes: (a) The overall longer duration when a fracture is loaded in progressive cycles. Since more time passes during the loading and unloading procedure, the fracture has longer time for compaction. Asperity deformation might be reduced and fracture consolidation is more effective. (b) Particle transportation causing partial blockage of fluid pathways. Unfortunately, we could not analyze the effluent on any changes in fluid composition or fines migration. (c) The observed stiffening effect could be sample-dependent. All samples showed the same initial fracture permeability and similar fracture stiffness evolution suggesting a good experimental comparability and reproducibility. In fact, it cannot be ruled out that the permeability deviations during CCL and PCL scenarios can be caused by any variations of the sample by either variation in fracture geometry, asperity strength, clay content, and so on.

During the hold phases, time-dependent permeability reductions are present, but with a limited impact on the overall permeability. Reductions were observed in the first loading cycle up to 30 MPa in the PCL experiments. In all subsequent cycles, permeability remained almost constant. In contrast, the CCL experiments showed a continuous decrease in permeability in all hold phases at 60 MPa (Figures 4b, 4d and 4f). Time-dependent permeability changes during the hold phases contribute by about 14%–15% to the total permeability changes caused by the pressure changes in the PCL experiments. In the CCL experiments creep contributes by about 0.5% although the permeability change was overall larger. We believe that the time frame of 20 min is too short to define a clear exponential or power-law behavior which is typical for mechanical creep for fracture closure (e.g., Im et al., 2018).

The roughness, aperture distribution, and contact-area control the plastic and elastic deformation of asperities, as well as the fluid flow in fractures (e.g., Cook, 1992; Kluge, Milsch, & Blöcher, 2017; Pyrak-Nolte & Morris, 2000; Zou et al., 2020). We did not find a change in roughness by cyclic loading experiments, similar to Yoshioka (1994). The roughness exponent was found to be similar before and after the experiment at frequencies above the length of the grain size. Most changes in surface topography are related to changes at the grain surface scale and/or to an elastic rearrangement of grains near contact-areas. However, calculating the mean aperture at various shear offsets using the post-experimental fracture surface scans (Figure 9b) and the aperture histograms (Figure 8) revealed a mechanical imprint. It is likely that fractures stiffness is not controlled by the bulk properties of rock, but by the grain properties. The self-affine roughness exponent is not affected by a complex mechanical loading history, proving its universality. The amount of aperture reduction did not exceed 0.12 mm comparing the mean aperture before and after the experiment. While plastic deformation of asperities seems to dominate the initial loading cycle with permanent fracture closure and permeability reduction, the following loading cycles lead to reversible fracture closure. The deformation process is dependent on the distribution of asperities (Zou et al., 2020). Hence, fracture stiffness depends on the shear offset and the resulting evolution of the fracture aperture. Larger or smaller offsets than the 0.5 mm from our experiments possibly lead to a different evolution of stiffness. Especially when considering a percolation threshold that leads to large permeability reductions. The contact-area and is dominated by the elastic properties of rock (Cook, 1992; Pyrak-Nolte & Morris, 2000) after the first loading cycle when most plastic deformation was done.

To be able to apply the experimental results to the field scale, the following aspects need to be considered. Creep should be considered as an important factor for larger systems due to possible temperature changes, rock-fluid interactions, or changes in stress distribution. Permeability can only be recovered by increasing the pore pressure in the fracture or an increased shear offset.

What we cannot address in this study is the mechanics behind each released pressure step and the dependency of a variety of geometries on the stress-paths dependent permeability. These are some potential aspects that should be considered in future studies.

4.3. Limitations of the Experimental Data

In the following, we review the assumptions made for our calculations and the limitations that emerged.

The fracture stiffness was calculated from the corrected fracture closure (Equation 11) by using the circumferential extensometer data (Equation 9) according to Bandis et al. (1983). The correction by the elastic strain impacts the slope and magnitude of the fracture closure and must be treated with caution. Regardless, this correction is crucial to be able to determine the strain caused by the deformation of a fracture only. Due to the cylindrical geometry with a diametrical fracture, the measured strain is a length phenomenon depending on the size of the fracture and the matrix surrounding it. Strain is therefore not homogeneous within the sample. The measured change in aperture (Equation 10) also depends on the local position of the extensometer along the sample and is controlled by local closure magnitudes. The roughness measurements (Section 3.5.1) showed that plastic asperity deformation takes place on the grain scale, although we consider bulk measurements of fracture closure and stiffness. Consequently, the aperture measurement must be considered as an indirect measurement.

Similar to the strain distribution, the hydrostatic confining pressure applied to the sample is not distributed equally throughout the sample. Depending on the fracture topography and sample geometry, the stress acting across sample and fracture varies. In the following we estimate the stress acting across the contact-area. From the aperture distribution (Figure 8) and the measured fracture closure, Δa, we calculated the evolution of the contact-area, R_c, as described in Section 3.5.2 (Figures 10a and 10b). Dividing the applied pressure by the computed contact-area, we obtained the stress acting on the fracture contacts at the respective applied effective pressure level (Figures 10c and 10d). During initial loading, the contact stress during the CCL experiment reached its peak of almost 700 MPa at about 4 MPa applied effective pressure and a decrease to about 450 MPa at 60 MPa (Figure 10c). The 450 MPa contact stress exceeds the uniaxial compressive strength of about 57 MPa for the Flechtingen sandstone as measured by Hassanzadegan et al. (2012). In all subsequent loading cycles, the contact stress was reversible without a peak. Most asperity damage is therefore done during initial loading at low applied effective pressures. Applying the same procedure to the PCL data, the contact stress increased until reaching the previous stress level (Figure 10d). The contact stress approached a limiting value of about 350–400 MPa at 60 MPa applied pressure. This suggests, that there is an universal contact stress level, in our case between 350 and 450 MPa, which controls the fracture stiffness at larger applied stresses. What this value represents, for example, the uniaxial compressive strength of a quartz grain, is not clear.

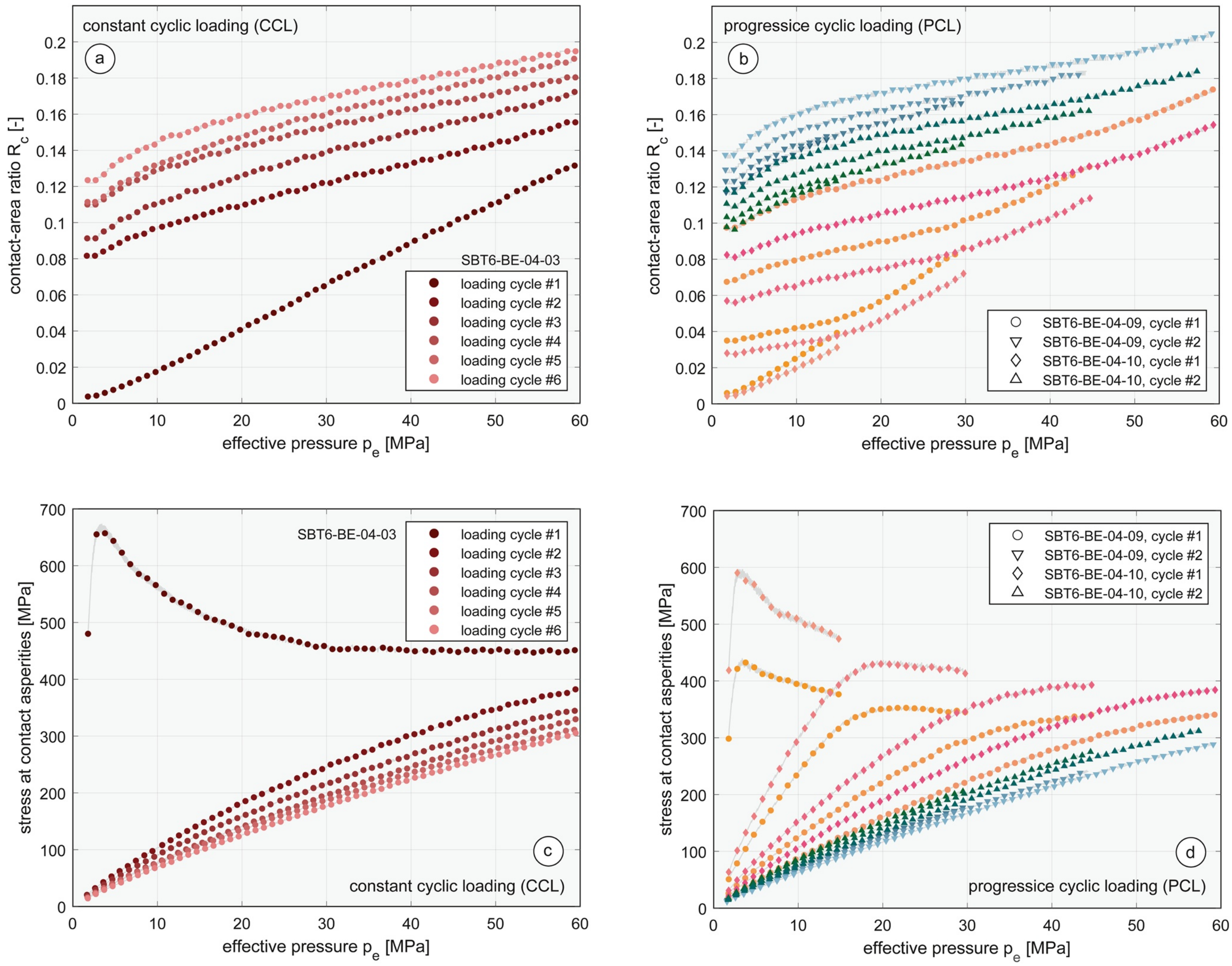

Figure 10. The fracture contact-area ratio (a, b) and the fracture contact-stress (c, d) at the respective applied effective pressure.

Although this shows the complex stress distribution within the sample, we assumed a homogeneous strain and stress distribution. We also consider fracture stiffness as a bulk property, albeit it is not controlled by the bulk properties of rock. Therefore, the uniaxial compressive strength of the bulk rock is not controlling the asperity strength as described by Milsch et al. (2016). These calculations and considerations reveal that we need to define clearly, what is actually measured and what is assumed in such laboratory experiments.

We further assume that the mechanical processes during cyclic loading (hysteresis) were not affected by the data acquisition rate (1 Hz). This is due to the low loading rate of 0.5 MPa/min and the measured displacement magnitudes within the mm-range. Studying rock samples with high-frequency loading rates and observations on a smaller spatial scale (nm-range) might require an adaption of the acquisition rate to properly determine all dynamic processes (Bella et al., 2021; Scalerandi et al., 2020).

5. Conclusions

In this study, we were able to demonstrate a novel experimental procedure to depict the fracture stiffness evolution during two different loading scenarios: CCL and PCL. Due to the high resolution of the deformation and pressure data, we were able to reveal a stress-memory effect of fracture stiffness during cyclic hydrostatic loading. Measuring the evolution of the hydraulic properties suggested that the permeability is dependent on the stress history.

Overall, we suggest the following conclusion to be made from our experimental results: (a) Initial loading of a fracture leads to a linear stiffness evolution. The linear trend is non-reversible when re-loading the fracture within the same stress range. The second and all subsequent cycles show a nonlinear and almost reversible behavior. The responsible micro-mechanical deformation modes (elastic, plastic, and elasto-plastic) in each phase remain to be evaluated. (b) When exceeding the previous stress level, the stiffness evolution turns from a nonlinear to a linear behavior. This suggests a stress-memory effect in fractures similar to the "Kaiser Effect" in intact rocks. (c) The permeability of a fracture is stress-path dependent. PCL potentially leads to a stiffening of the fracture at stress levels below the previous maximum stress. Therefore, the reduction caused by effective stress changes in fractured rocks could potentially be mitigated by a cyclic, step-wise pressure function. (d) The stiffening effect might also hold for larger-scale reservoirs where a reduction in productivity can be related to a decrease in pore pressure after stimulation and during production. We therefore suggest to verify cyclic or step-wise pressure reductions in field tests. (d) The fracture surface roughness above grain scale remains unchanged applying stress of up to 60 MPa. This supports the universality of the self-affine roughness exponent, since it is not affected by a complex mechanical loading history. Topography changes were indicated by a change in aperture distribution and a mechanical imprint, which reduces the self-propping effect at the given displacement.

Conflict of Interest

The authors declare no conflict of interest relevant to this study.

Data Availability Statement

In addition to being fully documented within this study, all experimental data were submitted to the GFZ Data Repository for public availability and can be accessed online (https://doi.org/10.5880/GFZ.4.8.2021.007; Kluge, Blöcher, Hofmann et al., 2021).

Acknowledgments
This project has received funding from the ReSalt project funded by the Federal Ministry for Economic Affairs and Energy (BMWi) under grant agreement no. 0324244C. Hannes Hofmann is grateful for the financial support from the Helmholtz Association's Initiative and Networking Fund for the Helmholtz Young Investigator Group ARES (contract number VH-NG-1516). Jean Schnittbuhl was supported by the LabEx G-EAU-THERMIE PROFONDE (ANR-11-LABX-0050) program. Open access funding enabled and organized by Projekt DEAL.

References

Akarapu, S., Sharp, T., & Robbins, M. O. (2011). Stiffness of contacts between rough surfaces. *Physical Review Letters*, *106*(20). https://doi.org/10.1103/Physrevlett.106.204301

Bandis, S., Lumsden, A., & Barton, N. (1983). Fundamentals of rock joint deformation. *International Journal of Rock Mechanics and Mining Sciences & Geomechanics Abstracts*, *20*(6), 249–268. https://doi.org/10.1016/0148-9062(83)90595-8

Bella, A. D., Scalerandi, M., Gliozzi, A., & Bosia, F. (2021). Adhesion and plasticity in the dynamic response of rough surfaces in contact. *International Journal of Solids and Structures*, *216*, 17–29. https://doi.org/10.1016/j.ijsolstr.2021.01.011

Blöcher, G., Reinsch, T., Hassanzadegan, A., Milsch, H., & Zimmermann, G. (2014). Direct and indirect laboratory measurements of poroelastic properties of two consolidated sandstones. *International Journal of Rock Mechanics and Mining Sciences*, *67*, 191–201. https://doi.org/10.1016/j.ijrmms.2013.08.033

Blöcher, G., Reinsch, T., Henninges, J., Milsch, H., Regenspurg, S., Kummerow, J., et al. (2016). Hydraulic history and current state of the deep geothermal reservoir groß schönebeck. *Geothermics*, *63*, 27–43. https://doi.org/10.1016/j.geothermics.2015.07.008

Boffa, J. M., Allain, C., & Hulin, J. P. (1998). Experimental analysis of fracture rugosity in granular and compact rocks. *The European Physical Journal - Applied Physics*, *2*(3), 281–289. https://doi.org/10.1051/epjap:1998194

Brown, S. R., & Scholz, C. H. (1986). closure of rock joints. *Journal of Geophysical Research*, *91*(B5), 4939. https://doi.org/10.1029/JB091iB05p04939

Candela, T., Renard, F., Klinger, Y., Mair, K., Schmittbuhl, J., & Brodsky, E. E. (2012). Roughness of fault surfaces over nine decades of length scales. *Journal of Geophysical Research*, *117*(B8). https://doi.org/10.1029/2011JB009041

Chen, Y., Liang, W., Lian, H., Yang, J., & Nguyen, V. P. (2017). Experimental study on the effect of fracture geometric characteristics on the permeability in deformable rough-walled fractures. *International Journal of Rock Mechanics and Mining Sciences*, *98*, 121–140. https://doi.org/10.1016/j.ijrmms.2017.07.003

Chen, Z., Narayan, S., Yang, Z., & Rahman, S. (2000). An experimental investigation of hydraulic behaviour of fractures and joints in granitic rock. *International Journal of Rock Mechanics and Mining Sciences*, *37*(7), 1061–1071. https://doi.org/10.1016/S1365-1609(00)00039-3

Cook, N. (1992). Natural joints in rock: Mechanical, hydraulic and seismic behaviour and properties under normal stress. *International Journal of Rock Mechanics and Mining Sciences & Geomechanics Abstracts*, *29*(3), 198–223. https://doi.org/10.1016/0148-9062(92)93656-5

Crawford, B. R., Tsenn, M. C., Homburg, J. M., Freysteinson, J. A., & Reese, W. C. (2016). Incorporating universal scaling of fracture stiffness and surface roughness effects for improved productivity prediction in naturally fractured reservoirs. *Paper presented at the 50th U.S. Rock Mechanics/Geomechanics Symposium* (Vols. 26–29).

Darcy, H. P. G. (1856). Les Fontaines publiques de la ville de Dijon. Exposition et application des principes á suivre et des formules 'a employer dans les questions de distribution d'eau, etc. V. Dalamont.

Greenwood, J. A., & Williamson, J. B. P. (1966). Contact of nominally flat surfaces. *Proceedings of the Royal Society of London Series A Mathematical and Physical Sciences*, *295*(1442), 300–319. https://doi.org/10.1098/rspa.1966.0242

Guo, H., Aziz, N., & Schmidt, L. (1993). Rock fracture-toughness determination by the Brazilian test. *Engineering Geology*, *33*(3), 177–188. https://doi.org/10.1016/0013-7952(93)90056-I

Hassanzadegan, A., Blöcher, G., Milsch, H., Urpi, L., & Zimmermann, G. (2014). The effects of temperature and pressure on the porosity evolution of flechtinger sandstone. *Rock Mechanics and Rock Engineering*, *47*(2), 421–434. https://doi.org/10.1007/s00603-013-0401-z

Hassanzadegan, A., Blöcher, G., Zimmermann, G., & Milsch, H. (2012). Thermoporoelastic properties of flechtinger sandstone. *International Journal of Rock Mechanics and Mining Sciences*, *49*, 94–104. https://doi.org/10.1016/j.ijrmms.2011.11.002

Hofmann, H., Blöcher, G., Milsch, H., Babadagli, T., & Zimmermann, G. (2016). Transmissivity of aligned and displaced tensile fractures in granitic rocks during cyclic loading. *International Journal of Rock Mechanics and Mining Sciences*, *87*, 69–84. https://doi.org/10.1016/j.ijrmms.2016.05.011

Hofmann, H., Zimmermann, G., Zang, A., & Min, K. B. (2018). Cyclic soft stimulation (CSS): A new fluid injection protocol and traffic light system to mitigate seismic risks of hydraulic stimulation treatments. *Geothermal Energy*, *6*(1). https://doi.org/10.1186/s40517-018-0114-3

Holcomb, D. (1993). General theory of the Kaiser effect. *International Journal of Rock Mechanics and Mining Sciences & Geomechanics Abstracts*, *30*(7), 929–935. https://doi.org/10.1016/0148-9062(93)90047-H

Im, K., Elsworth, D., & Fang, Y. (2018). The influence of preslip sealing on the permeability evolution of fractures and faults. *Geophysical Research Letters*, *45*(1), 166–175. https://doi.org/10.1002/2017GL076216

Kaiser, J. (1953). Erkenntnisse und folgerungen aus der messung von geräuschen bei zugbeanspruchung von metallischen werkstoffen. *Archiv für das Eisenhuttenwesen*, *24*(1–2), 43–45. https://doi.org/10.1002/srin.195301381

Kling, T., Vogler, D., Pastewka, L., Amann, F., & Blum, P. (2018). Numerical simulations and validation of contact mechanics in a granodiorite fracture. *Rock Mechanics and Rock Engineering*, *51*(9), 2805–2824. https://doi.org/10.1007/s00603-018-1498-x

Kluge, C., Blöcher, G., Barnhoorn, A., & Bruhn, D. (2020). Hydraulic-mechanical properties of microfaults in granitic rock using the punch-through shear test. *International Journal of Rock Mechanics and Mining Sciences*, *134*, 104393. https://doi.org/10.1016/j.ijrmms.2020.104393

Kluge, C., Blöcher, G., Hofmann, H., Barnhoorn, A., Schmittbuhl, J., & Bruhn, D. (2021). *Experimental data for permeability and stiffness measurements of fractured Flechtingen sandstone measured with a triaxial compression apparatus*. GFZ Data Services. https://doi.org/10.5880/GFZ.4.8.2021.007

Kluge, C., Blöcher, G., Barnhoorn, A., Schmittbuhl, J., & Bruhn, D. (2021). Permeability evolution during shear zone initiation in low-porosity rocks. *Rock Mechanics and Rock Engineering*. https://doi.org/10.1007/s00603-020-02356-0

Kluge, C., Blöcher, G., Milsch, H., Hofmann, H., Nicolas, A., Li, Z., & Fortin, J. (2017). Sustainability of fractured rock permeability under varying pressure. *Paper presented at the Poromechanics VI: Proceedings of the Sixth Biot Conference on Poromechanics*. https://doi.org/10.1061/9780784480779.148

Kluge, C., Milsch, H., & Blöcher, G. (2017). Permeability of displaced fractures. *Energy Procedia*, *125*, 88–97. https://doi.org/10.1016/j.egypro.2017.08.077

Lavrov, A. (2003). The kaiser effect in rocks: Principles and stress estimation techniques. *International Journal of Rock Mechanics and Mining Sciences*, *40*(2), 151–171. https://doi.org/10.1016/S1365-1609(02)00138-7

Lavrov, A. (2005). Fracture-induced physical phenomena and memory effects in rocks: A review. *Strain*, *41*(4), 135–149. https://doi.org/10.1111/j.1475-1305.2005.00233.x

Lockner, D. (1993). The role of acoustic emission in the study of rock fracture. *International Journal of Rock Mechanics and Mining Sciences & Geomechanics Abstracts*, *30*(7), 883–899. https://doi.org/10.1016/0148-9062(93)90041-B

Marache, A., Riss, J., & Gentier, S. (2008). Experimental and modelled mechanical behaviour of a rock fracture under normal stress. *Rock Mechanics and Rock Engineering*, *41*(6), 869–892. https://doi.org/10.1007/s00603-008-0166-y

Meakin, P. (1998). *Fractals, scaling and growth far from equilibrium* (Vol. 5). Cambridge University Press.

Milsch, H., Hofmann, H., & Blöcher, G. (2016). An experimental and numerical evaluation of continuous fracture permeability measurements during effective pressure cycles. *International Journal of Rock Mechanics and Mining Sciences*, *89*, 109–115. https://doi.org/10.1016/j.ijrmms.2016.09.002

Noël, C., Passelègue, F. X., Giorgetti, C., & Violay, M. (2019). Fault reactivation during fluid pressure oscillations: Transition from stable to unstable slip. *Journal of Geophysical Research: Solid Earth*, *124*(11), 10940–10953. https://doi.org/10.1029/2019JB018517

Pei, L., Blöcher, G., Milsch, H., Deon, F., Zimmermann, G., Rühaak, W., et al. (2016). Thermal strain in a water-saturated limestone under hydrostatic and deviatoric stress states. *Tectonophysics*, *688*, 49–64. https://doi.org/10.1016/j.tecto.2016.09.020

Pei, L., Hyun, S., Molinari, J., & Robbins, M. (2005). Finite element modeling of elasto-plastic contact between rough surfaces. *Journal of the Mechanics and Physics of Solids*, *53*(11), 2385–2409. https://doi.org/10.1016/j.jmps.2005.06.008

Persson, B. N. J. (2006). Contact mechanics for randomly rough surfaces. *Surface Science Reports*, *61*(4), 201–227. https://doi.org/10.1016/j.surfrep.2006.04.001

Persson, B. N. J. (2007). Relation between interfacial separation and load: A general theory of contact mechanics. *Physical Review Letters*, *99*(12). https://doi.org/10.1103/PhysRevLett.99.125502

Petrovitch, C. L., Nolte, D. D., & Pyrak-Nolte, L. J. (2013). Scaling of fluid flow versus fracture stiffness. *Geophysical Research Letters*, *40*(10), 2076–2080. https://doi.org/10.1002/grl.50479

Pyrak-Nolte, L. J. (1987). *Hydraulic and mechanical properties of natural fractures in low-permeability rock (Report LBL-22718)*. Lawrence Berkeley National Laboratory (LBNL).

Pyrak-Nolte, L. J. (1996). The seismic response of fractures and the interrelations among fracture properties. *International Journal of Rock Mechanics and Mining Sciences & Geomechanics Abstracts*, *33*(8), 787–802. https://doi.org/10.1016/S0148-9062(96)00022-8

Pyrak-Nolte, L. J., & Morris, J. (2000). Single fractures under normal stress: The relation between fracture specific stiffness and fluid flow. *International Journal of Rock Mechanics and Mining Sciences*, *37*(1–2), 245–262. https://doi.org/10.1016/S1365-1609(99)00104-5

Pyrak-Nolte, L. J., & Nolte, D. D. (2016). Approaching a universal scaling relationship between fracture stiffness and fluid flow. *Nature Communications*, *7*(1). https://doi.org/10.1038/ncomms10663

Raven, K., & Gale, J. (1985). Water flow in a natural rock fracture as a function of stress and sample size. *International Journal of Rock Mechanics and Mining Sciences & Geomechanics Abstracts*, *22*(4), 251–261. https://doi.org/10.1016/0148-9062(85)92952-3

Rutqvist, J. (2015). Fractured rock stress-permeability relationships from in situ data and effects of temperature and chemical-mechanical couplings. *Geofluids*, *15*(1–2), 48–66. https://doi.org/10.1111/gfl.12089

Scalerandi, M., Mechri, C., Bentahar, M., Bella, A. D., Gliozzi, A., & Tortello, M. (2020). Role of slow dynamics in fast dynamics ultrasonic measurements. *Communications in Nonlinear Science and Numerical Simulation*, *91*, 105452. https://doi.org/10.1016/j.cnsns.2020.105452

Schmittbuhl, J., Schmitt, F., & Scholz, C. (1995). Scaling invariance of crack surfaces. *Journal of Geophysical Research: Solid Earth*, *100*(B4), 5953–5973. https://doi.org/10.1029/94JB02885

Schmittbuhl, J., Vilotte, J. P., & Roux, S. (1995). Reliability of self-affine measurements. *Physical Review E*, *51*(1), 131–147. https://doi.org/10.1103/PhysRevE.51.131

Skurtveit, E., Sundal, A., Bjørnarå, T. I., Soldal, M., Sauvin, G., Zuchuat, V., et al. (2020). Experimental investigation of natural fracture stiffness and flow properties in a faulted CO_2 bypass system (Utah, USA). *Journal of Geophysical Research: Solid Earth*, *125*(7). https://doi.org/10.1029/2019JB018917

Terzaghi, K. (1925). *Erdbaumechanik Auf Bodenphysikalischer Grundlage*. F. Deuticke.

Thörn, J., Ericsson, L. O., & Fransson, Å. (2015). Hydraulic and hydromechanical laboratory testing of large crystalline rock cores. *Rock Mechanics and Rock Engineering*, *48*(1), 61–73. https://doi.org/10.1007/s00603-013-0538-9

Vogler, D., Amann, F., Bayer, P., & Elsworth, D. (2016). Permeability evolution in natural fractures subject to cyclic loading and gouge formation. *Rock Mechanics and Rock Engineering*, *49*(9), 3463–3479. https://doi.org/10.1007/s00603-016-1022-0

Wang, L., & Cardenas, M. B. (2016). Development of an empirical model relating permeability and specific stiffness for rough fractures from numerical deformation experiments. *Journal of Geophysical Research: Solid Earth*, *121*(7), 4977–4989. https://doi.org/10.1002/2016JB013004

Watanabe, N., Hirano, N., & Tsuchiya, N. (2009). Diversity of channeling flow in heterogeneous aperture distribution inferred from integrated experimental-numerical analysis on flow through shear fracture in granite. *Journal of Geophysical Research*, *114*(B4). https://doi.org/10.1029/2008JB005959

Witherspoon, P. A., Wang, J. S. Y., Iwai, K., & Gale, J. E. (1980). Validity of cubic law for fluid flow in a deformable rock fracture. *Water Resources Research*, *16*(6), 1016–1024. https://doi.org/10.1029/WR016i006p01016

Xia, C., Yue, Z., Tham, L., Lee, C., & Sun, Z. (2003). Quantifying topography and closure deformation of rock joints. *International Journal of Rock Mechanics and Mining Sciences*, *40*(2), 197–220. https://doi.org/10.1016/S1365-1609(02)00134-X

Yoshioka, N. (1994). The role of plastic deformation in normal loading and unloading cycles. *Journal of Geophysical Research*, *99*(B8), 15561. https://doi.org/10.1029/94JB00931

Zangerl, C., Evans, K., Eberhardt, E., & Loew, S. (2008). Normal stiffness of fractures in granitic rock: A compilation of laboratory and in-situ experiments. *International Journal of Rock Mechanics and Mining Sciences*, *45*(8), 1500–1507. https://doi.org/10.1016/j.ijrmms.2008.02.001

Zimmerman, R. W. (2008). A simple model for coupling between the normal stiffness and the hydraulic transmissivity of a fracture. *Paper presented at the 42nd US Rock Mechanics Symposium and 2nd US-Canada Rock Mechanics Symposium*.

Zou, L., Li, B., Mo, Y., & Cvetkovic, V. (2020). A high-resolution contact analysis of rough-walled crystalline rock fractures subject to normal stress. *Rock Mechanics and Rock Engineering*, *53*(5), 2141–2155. https://doi.org/10.1007/s00603-019-02034-w